UNIVERSIDADE DE SÃO PAULO

ESCOLA POLITÉCNICA

GABRIEL MIGLIANO SILVA

Modeling of uranium trioxide to uranium tetrafluoride conversion using a moving bed reactor

São Paulo
2021

GABRIEL MIGLIANO SILVA

Modeling of uranium trioxide to uranium tetrafluoride conversion using a moving bed reactor

Revised Version

Master Dissertation submitted to the Graduate Program in Chemical Engineering at the Escola Politécnica, Universidade de São Paulo, to obtain the degree of Master of Science

Field: Chemical Engineering

Advisor: Profa. Dra. Rita Maria de Brito Alves

São Paulo
2021

Este exemplar foi revisado e corrigido em relação à versão original, sob responsabilidade única do autor e com a anuência de seu orientador.

São Paulo, 11 de novembro de 2021.

Assinatura do autor: _____

Assinatura do orientador: _____

Catalogação-na-publicação

Silva, Gabriel Migliano
Modeling of uranium trioxide to uranium tetrafluoride conversion using a moving bed reactor / G. M. Silva -- versão corr. -- São Paulo, 2021.
78 p.

Dissertação (Mestrado) - Escola Politécnica da Universidade de São Paulo. Departamento de Engenharia Química.

1.Modeling 2.Uranium tetrafluoride 3.Moving bed reactor I.Universidade de São Paulo. Escola Politécnica. Departamento de Engenharia Química II.t.

SILVA, G. M. **Modeling of uranium trioxide to uranium tetrafluoride conversion using a moving bed reactor**. 2021. Dissertação (Mestrado) – Departamento de Engenharia Química, Universidade de São Paulo, São Paulo, 2021.

Approved in: 27/09/2021.

Examining Board

Prof. Dra.	Rita Maria de Brito Alves
Institution:	PQI-EPUSP
Judgement:	Approved
Dr.	José Carlos Bressiani
Institution:	IPEN
Judgement:	Approved
Prof. Dr.	Reginaldo Guirardello
Institution:	FEQ-UNICAMP
Judgement:	Approved

ACKNOWLEDGEMENTS

To my wife, Alessandra de Carvalho Reis, for all the love, support and understanding, even in the most difficult times of my life.

To my family members, for having given me access to a great education, and for always taking care of me with everything they could.

To my advisor, Profa. Dra. Rita Maria de Brito Alves, for having trusted in my capacity as student, and for all the important teachings shared.

To my peers and superiors in Marinha do Brasil, for giving me support and allowing me to enroll in this graduation course.

And, finally, to God, for providing me with opportunities and challenges that have contributed to my personal and professional growth.

“The greater our knowledge increases, the more our ignorance unfolds.”

John F. Kennedy

RESUMO

SILVA, G. M. **Modeling of uranium trioxide to uranium tetrafluoride conversion using a moving bed reactor**. 2021. Dissertação (Mestrado) – Departamento de Engenharia Química, Universidade de São Paulo, São Paulo, 2021.

A fim de cumprir com a Estratégia de Defesa Nacional, a Marinha do Brasil está atualmente desenvolvendo um projeto para a construção de submarinos de propulsão nuclear, que usam pastilhas de óxido de urânio como combustível. Uma das etapas de manufatura para esse composto químico é a conversão de trióxido de urânio em tetrafluoreto de urânio, usando fluoreto de hidrogênio, o que ocorre em um reator de leito móvel, também chamado de forno. Motivado pela escassez de estudos na literatura e na necessidade apresentada pela Marinha do Brasil, este trabalho tem o objetivo de desenvolver um modelo para a conversão de UO_3 em UF_4 em um reator de leito móvel usando o software MATLAB®. Esse modelo utiliza um sistema de equações diferenciais parciais e condições de contorno obtidas da literatura, bem como a geometria do reator do projeto da Marinha do Brasil, o qual é então resolvido usando um método de Newton das sub-rotinas do software. Os resultados, como as densidades dos sólidos, concentrações de gases, e gráficos de temperatura e pressão, são obtidos e discutidos neste trabalho, mostrando compatibilidade com a literatura atual.

Palavras-chave: Modelagem. Tetrafluoreto de Urânio. Reator de Leito Móvel.

ABSTRACT

SILVA, G. M. **Modeling of uranium trioxide to uranium tetrafluoride conversion using a moving bed reactor**. 2021. Dissertação (Mestrado) – Departamento de Engenharia Química, Universidade de São Paulo, São Paulo, 2021.

In order to comply with the National Defense Strategy, the Marinha do Brasil is currently developing a project for the construction of nuclear-driven submarines, which uses enriched uranium oxide pellets as fuel. One of the manufacturing steps for this chemical compound is the conversion of uranium trioxide to uranium tetrafluoride using hydrogen fluoride, which occurs in a moving bed reactor, also called a furnace. Motivated by the scarcity of studies in the literature and the need presented by the Marinha do Brasil, this work aims to develop a model for the conversion of UO_3 into UF_4 in a moving bed reactor using MATLAB® software. This model utilizes a set of partial differential equations and boundary conditions obtained from the literature, as well as the reactor geometry from the Marinha do Brasil project, which is then solved using a Newton method from the software subroutines. Results, such as solids densities, gas concentrations, temperature and pressure plots, are obtained and discussed herein, showing compatibility to the literature.

Keywords: Modeling. Uranium Tetrafluoride. Moving Bed Reactor.

LIST OF FIGURES

LIST OF TABLES

LIST OF ABBREVIATIONS AND SYMBOLS

Throughout this work, symbols expressed in normal letters denote scalar values, while symbols in *italics* represent a coordinate or indices. Also, symbols in **bold** represent average constant values, while symbols in *italics* represent an index or a coordinate. The units for each symbolic term are presented after their definition (usually by a comma), and, if no unit is shown, this means the term is dimensionless.

ABBREVIATIONS

CSTR	Continuous Stirred Tank Reactor
EEZ	Exclusive Economic Zone
PDE	Partial Differential Equation
PFR	Plug Flow Reactor
USEXA	Unidade Piloto de Hexafluoreto de Urânio

NOTATIONS – LATIN LETTERS

A	area, m^2
c_i	concentration of species *i*, $mol.m^{-3}$
c_t	total gaseous molar concentration, $mol.m^{-3}$
C_p	heat capacity at constant pressure, $J.kg^{-1}.K^{-1}$ (solids) or $J.mol^{-1}.K^{-1}$ (gases)
D	dispersion coefficient, $m^2.s^{-1}$
d	diameter, m
Ea_j	activation energy of reaction *j*, $J.mol^{-1}$
F	molar flow, $mol.s^{-1}$
h	convective heat transfer coefficient, $W.m^{-2}.K^{-1}$
h_{ext}	convective heat transfer coefficient external to the furnace, $W.m^{-2}.K^{-1}$
$k_{0,j}$	pre-exponential factor of the specific velocity of reaction *j*, units vary depending on reaction order
K_{eq}	thermodynamic equilibrium constant

L	length, m
M_i	molecular weight of species *i*, $kg.mol^{-1}$
n	CSTR number
Nu	Nusselt number
p	absolute pressure, Pa
Pe	Péclet number
Pr	Prandtl number
R	gas constant, $J.mol^{-1}.K^{-1}$
r	radial coordinate, m
r_j	rate expression for reaction *j*, $mol.s^{-1}.m^{-3}$ of bed
R_0	tube radius, m
Re	Reynolds number
Sc	Schmidt number
T	temperature, K
T_{ext}	ambient temperature, K
T_0	reference temperature, K
u	superficial velocity, $m.s^{-1}$
U	overall heat transfer coefficient, $W.m^{-2}.K^{-1}$
v	diffusion volume for the Fuller-Schettler-Giddings equation
V	internal volume of the equipment, m^3
w_i	mass fraction of species *i*
x_i	molar fraction of species *i*
Xj	conversion of reaction *j*
$y_{0,H2}$	molar fraction of H_2 in the NH_3 feed
z	axial coordinate, m

NOTATIONS – GREEK LETTERS

β	angle between axis and blades in the horizontal section, radians
δ_j	normalized net difference between stoichiometric coefficients of reaction *j*. For the cracking reaction, $\delta_{cr} = 1$
ΔCp_j	specific heat variation of reaction *j*, $J.mol^{-1}.K^{-1}$
$\Delta H_{r,j}$	enthalpy of reaction *j*, $J.mol^{-1}$
$\Delta H^{298}_{r,j}$	enthalpy of reaction *j* at 298 K, $J.mol^{-1}$
ε_b	bed porosity
ε_p	pellet porosity
ε_t	thermal emittance
λ	thermal conductivity, $W.m^{-1}.K^{-1}$
λ_{eff}	overall effective thermal conductivity, $W.m^{-1}.K^{-1}$
μ	dynamic viscosity, $kg.m^{-1}.s^{-1}$
θ	azimuthal coordinate, degrees
υ_i	volume flow of species *i*, $m^3.s^{-1}$
ρ_i	weight concentration of species *i*, $kg.m^{-3}$ of bed
ρ_t	apparent (total) weight concentration of the solid, $kg.m^{-3}$ of bed

SUBSCRIPTS

0	initial condition or at the entrance
a	axis
aq	muffle surrounding the zone
aqb	between the bottom of the zone and the muffle
aqt	between the top of the zone and the muffle
b	blades
buf	buffer zone
cr	cracking reaction
CSTR	CSTR

g	gaseous phase
hf	hydrofluorination reaction
hfs	secondary Hydrofluorination reaction
hhz	horizontal hydrofluorination zone
H_2	hydrogen gas
HF	hydrogen fluoride (or fluoridric acid)
H_2O	water vapor
i	species
j	reaction
muf	ammonia heating muffle
N_2	nitrogen gas
NH_3	ammonia
O_2	oxygen gas
p	pellet
pi	pitch (distance between blades)
r	radial direction (*r* coordinate)
red	reduction zone
red1	reduction reaction of UO_3 to U_3O_8 (first reduction)
red2	reduction reaction of U_3O_8 to UO_2 (second reduction)
s	solid phase
UF_4	uranium tetrafluoride
UO_2	uranium dioxide
UO_2F_2	uranyl fluoride
UO_3	uranium trioxide
vhz	vertical hydrofluorination zone
w	wall
z	axial direction (*z* coordinate)

CONTENTS

1. INTRODUCTION

"Amazônia Azul" is the name given to the Brazilian ocean area, due to its comparative size to the Amazon Rainforest, representing an area of 4,500,000 km^2, formed by more than 3,000,000 km^2 of Exclusive Economic Zone (EEZ) and more than 960,000 km^2 of continental platform. Together, these maritime spaces correspond to 52% in size of continental lands (1). A map showing this region can be seen in **Figure 1**, in light blue and dark blue color.

Figure 1 - Region delimited by "Amazônia Azul" in national territory.

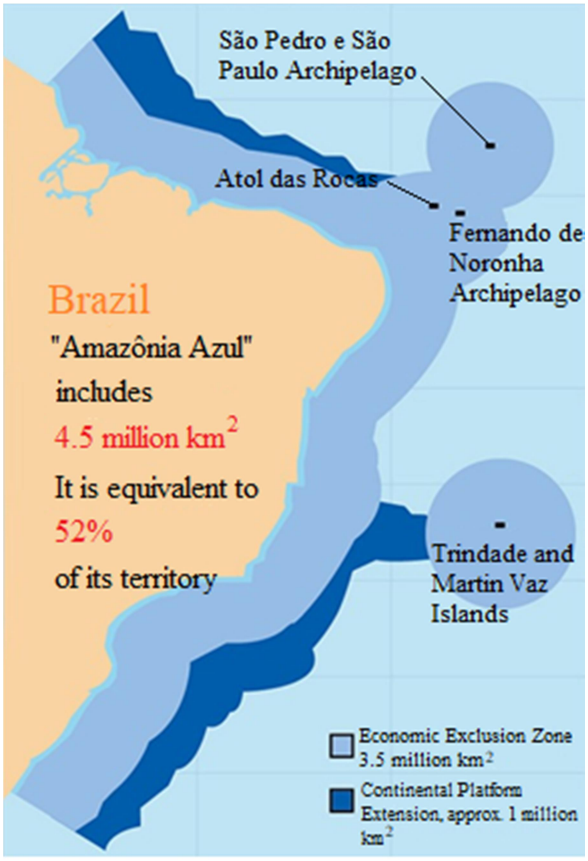

Source: Adapted from (1).

The project and building of the Brazilian nuclear-driven submarine is aimed to comply with the policies established in the National Defense Strategy, among them, the proactive defense of "Amazônia Azul", thus adding a new dimension to the national Naval Power. The possession of this new naval asset would contribute significantly to secure the sovereignty in Brazilian jurisdictional waters, ensuring dissuasion capacities and denial of sea use (2).

The construction of the submarines is being assisted by French collaborators, except for the nuclear reactor and associated uranium fuel-cycle technology, which is being developed

by Marinha do Brasil. When completed, they will be larger than submarines of classes Scorpène (in which its design would be based), Barracuda and Rubis (3).

In this kind of submarine, a nuclear reactor is used as energy source, and the generated heat is used to vaporize water, making it possible to employ this steam in turbines that can activate electric generators or the drive shaft of the vessel. Differently than conventional submarines, the nuclear ones have high mobility and, thus, are fundamental for distant ocean (deep) water defense. Hence, it can be said that the autonomy of nuclear-driven submarines is limited only by the physical and psychological resistance of its crew and its supply stock. Also, this energy source confers discretion to nuclear-driven vessels, in comparison to conventional energy-driven vessels, whose combustion engines present considerable noise generation.

In order to power the nuclear reactors, uranium oxide (UO_2) pellets, which are encased in metal tubes to form fuel rods that are arranged into a fuel assembly, are used. The set of industrial operations that encompass all stages of the fuel usage, since uranium ore mining to the disposal of radioactive waste, is called the nuclear fuel cycle (4) and its stages can be seen in **Figure 2**. In some cases, such as the Brazilian nuclear fuel cycle, the operations indicated by a red arrow are absent, as they are not mentioned in the Country Nuclear Fuel Cycle Profiles (5).

Figure 2 – Simplified diagram of the nuclear fuel cycle.

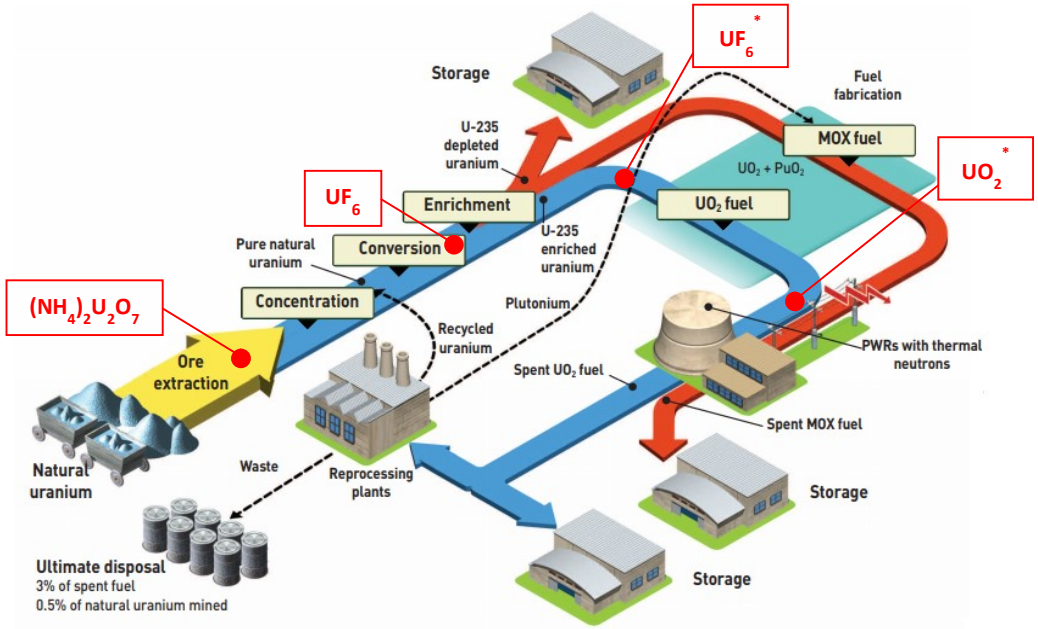

Source: Adapted from (4).

As seen in **Figure 2**, the concentrate uranium has to be converted to uranium hexafluoride (UF_6), a gas used in the enrichment step. However, this conversion is a two-stage process: in the first stage, the concentrate is converted into uranium tetrafluoride (UF_4), a granular green salt, and, in the second stage, this compound is converted into uranium hexafluoride through fluorination (6). One of the steps in the first stage is the conversion of uranium trioxide (UO_3) in uranium tetrafluoride, occurring in a single moving bed reactor, which is the focus of this work.

In Brazil, there is a facility in development stage for UF_6 production installed in the municipality of Iperó/SP and owned by Marinha do Brasil (Unidade Piloto de Hexafluoreto de Urânio - USEXA), in which the conversion takes place. Other facilities for UF_6 production around the world are presented in **Table 1**:

Table 1 – Facilities for UF_6 production around the world

Operator	Country	Location	Capacity (tU/yr)
Industrial Scale			
Cameco [1]	Canada	Port Hope, ON	12,500
Comurhex (AREVA) [2]	France	Malavesi and Pierrelatte	15,000
Rosatom [1]	Russia	Seversk	12,500
CNNC [1]	China	Lanzhou	5,000
Honeywell (Coverdyn) [2]	United States	Metropolis, IL	15,000
Plants Small-scale or "Pilot" Plants			
AEOI	Iran	Isfahan	~200
BARC	India	Trombay	(N/A)
CNEA	Argentina	Rio Negro	(N/A)
IPEN	Brazil	São Paulo	~100
(N/A)	North Korea	(N/A)	(N/A)
CPC	Pakistan	Dera Ghazi Khan	(N/A)

Source: Adapted from (7).
(N/A) = information not available.
UF_6 produced via: [1] "Wet" route; [2] "Dry" route.

Among all the facilities cited in **Table 1**, only the one operated by Comurhex (AREVA) in Malavesi, France uses a similar reactor than the one installed in USEXA ("dry route"), while other plants employ other processes for UF_4 production, such as the "wet route" (7). These processes will be explained in more details in subsequent sections.

Although some works have been published regarding the modeling of the conversion of UO_3 in UF_4 in a moving bed reactor for the "dry route", they do not provide the code used for the model and are not very recent. Thus, there is still need for a model that can represent the environment inside the moving bed reactor, justifying the development of this work.

1.1. OBJECTIVES

The main objective of this work is the formulation of a model able to correctly represent the mass, momentum and energy balances inside the moving bed reactor in which the conversion to UO_3 in UF_4 occurs.

The specific objectives can be described as follows:

▫ Develop a model in MATLAB®, describing the conversion of UO_3 to UF_4, including mass, momentum and energy balances, in a moving bed reactor;

▫ Replace correlations in the developed model in order to include more recent studies, thus obtaining a different model; and

▫ Compare the model obtained with data from the literature, in order to validate it.

1.2. STRUCTURE

Finally, this study is structured in the following manner:

▫ Chapter 1 introduces this work, as well as its justification, objective and structure;

▫ Chapter 2 presents background information, that is, expands the introduction by including more details regarding the reactor, which is the focus of this work, and other processes for UF_4 production;

▫ Chapter 3 describes the literature review of the studies already performed in the field of modeling this particular equipment and the reactions that occur inside it;

▫ Chapter 4 outlines the method that shows the steps for the model formulation and validation;

▫ Chapter 5 shows the results of this work, as well as a discussion for the obtained model; and

▫ Chapter 6 closes this work with its conclusions and suggestions for future works in the field.

2. BACKGROUND

This section provides information regarding the chemical reactions that occur during the conversion of uranium trioxide to uranium hexafluoride, as well as some examples of its industrial scale production process in some plants. A more detailed description of the furnace itself, such as its individual sections and its operation, is also presented.

2.1. PROCESSES FOR UF_4 PRODUCTION

The compound UF6 can be produced by the reaction of virtually any uranium compound with elemental fluorine at elevated temperatures. Although one can assume that the fluorine gas (F2) is used directly to such an end, its expensive production costs and hazardous nature encouraged researchers to find an alternative and safer route, which consists in the conversion of the uranium oxide to a fluorinated form with hydrogen fluoride (HF) before performing the fluorination, according to the set of unbalanced chemical reactions below:

$$\text{Step 1 – Reduction: } UO_3 + H_2 \rightarrow UO_2 + H_2O$$

$$\text{Step 2 – Hydrofluorination: } UO_2 + HF \rightarrow UF_4 + H_2O$$

$$\text{Step 3 – Fluorination: } UF_4 + F_2 \rightarrow UF_6$$

This approach considerably reduces F_2 consumption, since fluorination is partially done by HF (8). However, this presents the drawback that, if HF somehow comes in contact with unreacted UO_3 from Step 1, it will generate uranyl fluoride (UO_2F_2) as an undesired product, thus, control of the reduction reaction must be strict in order to maximize UF_4 yield.

Nowadays, there are two routes for producing UF_6: a “wet” route, in which yellowcake is dissolved and purified using solvent extraction and then converted in a series of denitration, reduction, hydrofluorination, and fluorination steps, and the “dry” route, where the feed is fairly pure, omitting the dissolution and solvent extraction steps, and including a fractional distillation step for final purification (9). The former is widely used in the industry, while only in a factory installed in Metropolis, IL performs the “dry route” (7).

2.1.1. UF_4 production at Cameco plant

The production of UF_6 through the "wet" route in Canada is divided in two plants, both operated by Cameco Corporation: one that comprises the uranium oxide concentrate (yellow cake) refining to UO_3 powder, located in Blind River, ON, and another, installed on Port Hope, ON, that converts it to UF_4 and, subsequently, to UF_6.

After receiving the yellow cake powder from the mines, the process starts with the dissolution with nitric acid in order to produce a uranyl nitrate solution, which, after a maturation step in low agitation, deposits insoluble material, such as silica. Then, this solution is purified using solvent extraction by TBP using a kerosene-type diluent in three absorption stages: extraction, scrubbing (impurity washing) and reextraction. The resulting solution is heated, concentrated and later thermally decomposed in stirred pots to form UO_3 powder, which, in turn, is stored in containers that are shipped to the other Cameco facility in Port Hope. The recycling of many compounds, such as water and nitric acid (in form of concentrated nitrogen oxide fumes) is possible (7). **Figure 3** presents a simplified diagram for the first step of the UF_6 production process:

Figure 3 – Diagram for the Cameco yellow cake refining plant

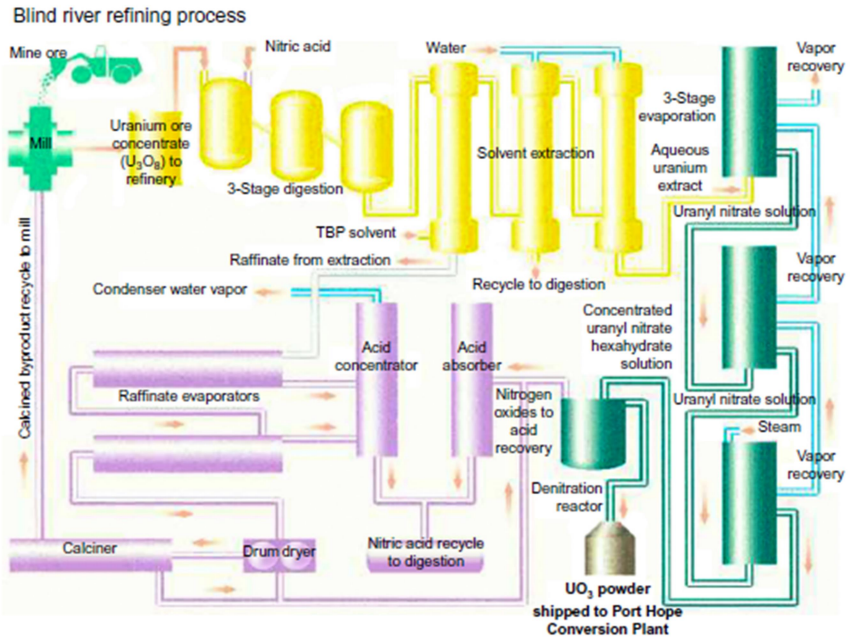

Source: (7).

The second part of the conversion process starts with the reduction of the UO_3 powder, which is done by pulverizing it into a fluid bed reactor, forming another oxide - UO_2. This powder is then fed into slurry reactors with water and preheated hydrofluoric acid for hydrofluorination, producing UF_4, that, in turn, is dried and fluorinated in flame reactors to UF_6 in a subsequent step of the process (7). A simplified diagram for this part of the process is shown in **Figure 4.**

Figure 4 – Diagram for the Cameco conversion plant

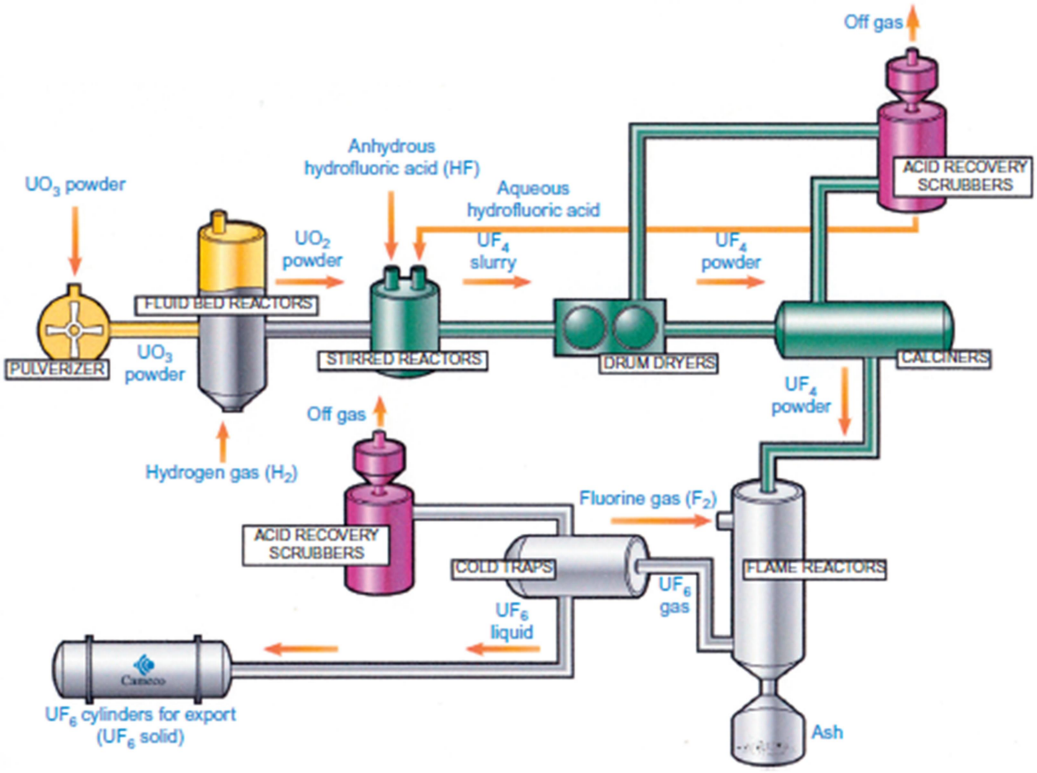

Source: (7).

2.1.2. UF_4 production at Comurhex plant

The facility operated by Comurhex/AREVA located in Malavesi, France, uses a configuration for TBP solvent extraction (column contactors) similar to the Cameco plant. One key difference is that this process involves evaporation and then precipitation of the concentrate uranium to make ammonium diuranate (ADU), which is dried and calcinated in a kiln to UO_3. The subsequent reduction to UO_2 and hydrofluorination to UF_4 are performed in a single moving bed or lit courant (LC) reactor, which uses ammonia and anhydrous HF as reactants, producing UF_4 as a green solid, which, in turn, is stored in vessels for shipping to

the UF_6 conversion facility in Pierrelatte, France (7). An outline of the Comurhex refining process in the Malavesi facility is shown in **Figure 5.**

Figure 5 – Diagram for the Comurhex plant in Malavesi

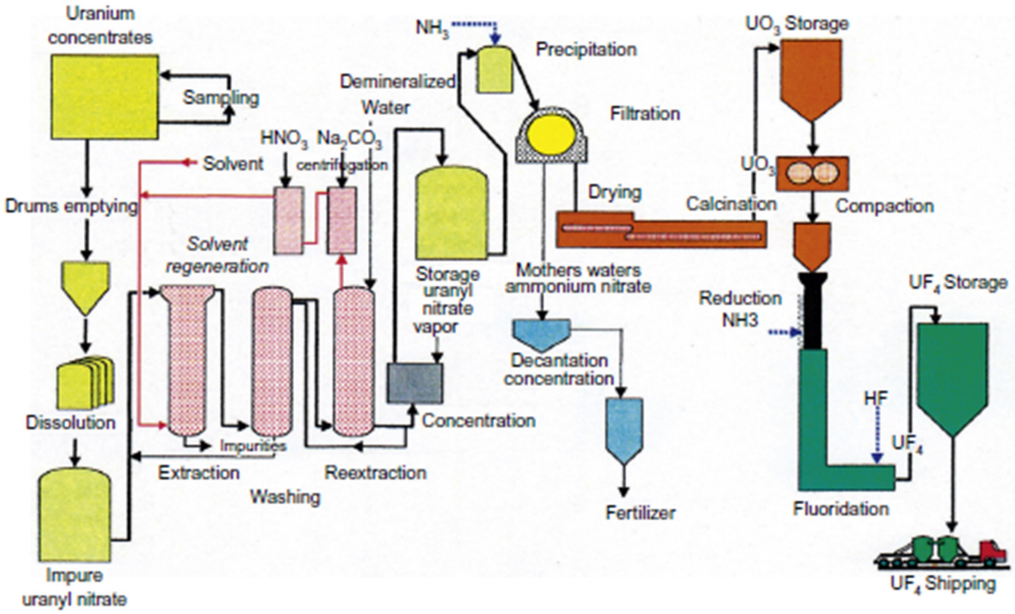

Source: (7).

2.2. CHARACTERISTICS OF THE MOVING BED REACTOR

The moving bed reactor object of this work is similar to the one that operates in the Comurhex facility, with some minor changes. Thus, this section aims to describe the different zones along this equipment, as well as the reactions that occur inside it, and its operation method.

2.2.1. General description and operation

The moving bed reactor (sometimes referred to as furnace or kiln) is a series of cylinders in the shape of an “L” that can be divided in two modules: a vertical one and a horizontal one, and these parts can be further divided into zones, each one with their own features (10). An increase of diameter between each zone is foreseen in order to accommodate

changes in solids density along the system. A schematic, without including instrumentation items, is presented in **Figure 6**.

Figure 6 – Schematic for the moving bed reactor

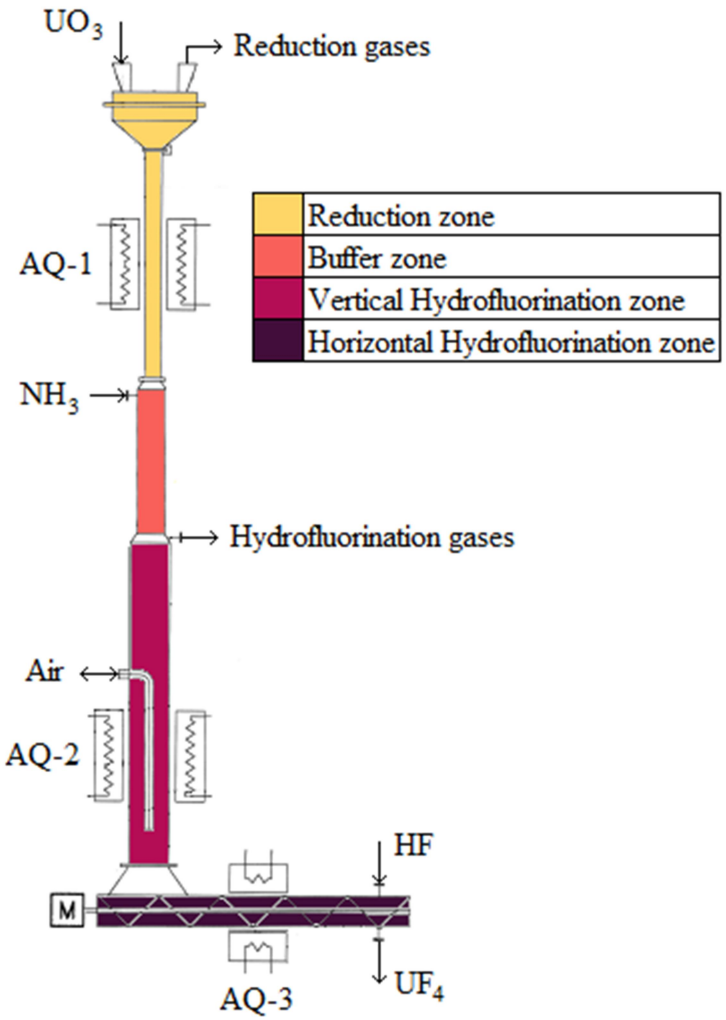

While the solids pass through the vertical module by gravity assisted by electrical vibrators, the gases flow through the opposite direction. This countercurrent setting is also applied in the horizontal part; however, the solids are transported from the left to the right end using a screw.

In order to perform the conversion, the following sequence must be adopted:

1) the system is purged with nitrogen (N_2) before the reactants are fed, the concentration of oxygen (O_2) must be smaller than 1% in the whole system in

which the reactor is connected. This step must not be interrupted, and maintained throughout the whole process;

2) the modules are completely filled with UF_4. UO_3 may be used in the exceptional case of stock shortage, but it will take longer for the reactor to achieve a steady state and, thus, generate a product within specifications;
3) the muffles AQ-1, AQ-2 and AQ-3 are turned on;
4) after achieving the muffles' set temperature, NH_3 and HF are fed into the system. Air is also allowed flowing through the heat exchanger in the vertical hydrofluorination zone; and
5) finally, UO_3 is fed into the reactor, and, simultaneously, the screw is powered on, allowing the solids to flow and the reactions to start.

2.2.2. The reduction zone

In the reduction zone, UO_3 is fed at the top (which represents the upper extremity of the furnace), while NH_3 is fed at the bottom, joined by a fraction of the gases of the hydrofluorination zone (non-reacted and by-products, such as HF and H_2O vapor). This ammonia stream enters the reactor at high temperature, but, since the average temperature in this zone is even higher (approximately between 600 ºC and 700 ºC), it is decomposed into H_2 and N_2 in a cracking reaction, which, in turn reduce UO_3 to U_3O_8 and then U_3O_8 to UO_2 through a reduction reaction, with the second reduction only beginning after the UO_3 is entirely converted to U_3O_8. UO_3 can also undesirably react with HF that comes from the hydrofluorination zone, generating UO_2F_2 as an inert byproduct in a parasitic reaction known as secondary hydrofluorination (10).

In summary, the following reactions occur in this zone:

Cracking: $2\ NH_3\ (g) \rightarrow N_2\ (g) + 3\ H_2\ (g)$

Calcination: $3\ UO_3\ (s) \rightarrow U_3O_8\ (s) + ½\ O_2\ (g)$

Reduction 1: $3\ UO_3\ (s) + H_2\ (g) \rightarrow U_3O_8\ (g) + H_2O\ (g)$

Reduction 2: $U_3O_8\ (s) + 2\ H_2\ (g) \rightarrow 3\ UO_2\ (s) + 2\ H_2O\ (g)$

Secondary Hydrofluorination: $UO_3\ (s) + 2\ HF\ (g) \rightarrow UO_2F_2\ (s) + H_2O\ (g)$

The reduction and hydrofluorination reactions are highly exothermic, which is a problem, since extreme temperatures must be avoided in order to prevent oxide sintering and operational instabilities. Cracking and calcination reactions are endothermic. In order to supply heat for the high temperatures required, a muffle (AQ-1) partially surrounds this zone. Temperature is carefully controlled with thermocouples installed in different locations throughout the bed in the whole reactor, so that local hot spots, which can soften the pellets and clog the equipment, may be avoided. In this section, it is expected that the cracking and reduction reactions are completed due to high temperatures.

2.2.3. The buffer zone

This zone acts as a transition between the reduction and the hydrofluoration zones. Also, the buffer zone shares the same reactions that occur in the reduction zone. Since there are no muffles here, a drastic temperature drop is expected (with temperatures typically below 300ºC), which does not kinetically favor any of the reactions. Thus, UO_2 conversion must be finalized before entering here, or else the remaining UO_3 will produce UO_2F_2 as undesired product in the next zones.

2.2.4. The vertical hydrofluorination zone

In this zone, descending UO_2 pellets react with a counter-flow of gaseous hydrogen fluoride (HF) to produce UF_4 in a reaction known as hydrofluorination, described as follows:

Hydrofluorination: $UO_2\,(s) + 4\,HF\,(g) \leftrightarrow UF_4\,(s) + 2\,H_2O\,(g)$

This reaction is also very exothermic, so a compromise must be found for a high temperature to ensure a high conversion degree for UF_4, but not enough to bring instabilities in the operation (between 300 ºC and 600 ºC).

Also, unlike other reactions listed in this work, the hydrofluorination is reversible, with extremely high temperatures favoring UF_4 hydrolyzation. Due to these factors, the temperature in this zone is carefully controlled by using a muffle (AQ-2) to increase the temperature and also an air-cooled internal coaxial heat exchanger to reduce it. Other reactions do not need to be considered in the vertical hydrofluorination zone, mostly due to the absence of reactants (H_2 for the reductions and UO_3 for the secondary hydrofluorination) (10).

At the top of this zone, a fraction of the hydrofluorination gases (mostly comprised of H_2O and unreacted HF), which is a parameter in the model, is removed from the reactor in order to reduce the quantity of HF that comes in contact with unreacted UO_3 in the reduction and buffer zones.

2.2.5. The horizontal hydrofluorination zone

In this final zone, the hydrofluorination reaction is completed, and the solid, which enters at the left extremity, leaves the furnace as UF_4 by using an Archimedes type screw to extract it at the end of the tube. The gaseous reactant HF is inserted at the right end of this zone, sometimes diluted in N_2, and flows counter-currently in relation to the solid.

Similarly to the vertical hydrofluorination zone, only the hydrofluorination reaction will be contemplated. A muffle (AQ-3) partially surrounds the reactor in this zone, in order to provide energy for setting a high enough temperature. The range of temperatures in this zone is the same of the previous one.

3. LITERATURE REVIEW

This section presents an overview of the existing models for the conversion process of the specific furnace, which is object of this work, as well as models for similar reactors and production methods. It also provides information regarding the current knowledge of the individual reactions that occur during this process.

3.1. EXISTING MODELS FOR UF_4 PRODUCTION

Since the nuclear fuel production in the world is closely tied to the national nuclear weapons program of their respective country, which contains only classified information, the literature regarding UF_4 production is scarce – only four articles describing the modeling of a complete moving bed reactor (and another for a specific part of this equipment) for this end exist.

The first set of articles by Dussoubs et al. (10, 11), describes a mathematical model of a moving bed reactor that has an identical structure of the one described in this work, except for the presence of a muffle in the vertical hydrofluorination zone (AQ-2). The steady-state two-dimensional model uses cylindrical coordinates *r* for radial distances and *z* for axial distances in the vertical module, with origins in the symmetry axis and the bottom of the hydrofluorination zone, respectively. Since the geometry in the horizontal zone is complex due to the presence of the Archimedes screw, the model approximates the horizontal hydrofluorination zone with a series of CSTR reactors for each empty space between blades ("pitch"), where the gas comes in contact counter-currently with the solid. The model describes the solid and gas flow, heat transfer by conduction, convection and radiation, as well as the pressure drop and various chemical reactions in the different zones, and its outputs are the apparent weight concentration of the solid, molar concentration of all solid species, total gas concentration, molar concentration of all gaseous species and total gas pressure, in all points of the furnace, as well as cooling fluid (air) temperature in all points of the heat exchanger. The balance and constitutive equations form a system of PDEs, which is solved numerically using the finite volume method for the vertical module and from one reactor to another for the horizontal module. Finally, the model is validated comparing calculated temperature data with temperatures measured in certain points of the moving bed reactor

operated by Comurhex, in Malavesi, France. Calculations also show that the whole process is controlled by intramolecular diffusion.

Dussoubs et al. (12) also presents and discusses detailed results of the simulation obtained in the article previously described. Such results include, for example, profiles of temperature, chemical reaction rates and fractions of gases and solid species in the different parts of the furnace. The influence of various operating parameters was also studied and results were compared against a reference case, obtained using a standard set of industrial operating parameters of the moving bed furnace. Each effect of varying a parameter is described by the following items:

▫ *Mean pellet diameter*: While the reference case includes a pellet size decrease in the reduction zone as a linear function of the mass fraction of UO_2, the new simulation keeps the mean pellet diameter constant throughout the reactor. This effective increase in pellet diameter resulted in a decrease in the reduction reaction rate, which, in turn, generated a cascade effect that culminated in a significant decrease in the mass fraction of UF_4.

▫ *Fraction of gas entering in the reduction zone*: The increase in the flow rate of hydrofluorination gases that enter in the reduction zone brings about a better cooling of the reduction zone by increased convection, reducing, thus, the reaction rates and the mass fraction of the desired product.

▫ *Gas flow rate fed in the horizontal hydrofluorination zone*: An increase in the HF flow rate by 20%, when compared to its reference value (slightly above the stoichiometric amount), favors the conversion in the hydrofluorination zone. However, the mass fraction of UF_4 at the exit of the reactor is lower than the reference case. This behavior is due to the fact that since more gas flows to the reduction zone, the temperature decreases and a less complete reduction is expected.

▫ *Input cracked fraction of NH_3*: In the reference model, a fraction of the ammonia is cracked in N_2 and H_2 due to its high temperature feed. By decreasing this value, the temperature becomes insufficient to initiate cracking inside the furnace, resulting in an incomplete reduction, and consequently, hydrofluorination.

The article also concludes with the following remarks:

1) the hypotheses of equal gas and solid temperatures and the use of the law of additive characteristic times for modeling the reaction rates has been ascertained, when comparing with results using a more complete and robust grain model;

2) the reduction of moving bed width by decreasing the radial temperature and solid composition gradients has proven to be efficient to optimize the conversion; and
3) in the reduction zone, the location of the first reduction quickly occurs at the very top of the furnace, while the second reduction is slower, taking place in a wider region and, depending on the parameters, may not be fully completed. For the hydrofluorination zones, calculations show that UF_4 conversion is very slow in large zones, which can be attributed to a thermodynamic limitation at high temperature and strong radial temperature gradients.

The model developed by Dussoubs et al. (10) presents some drawbacks, such as the use of the law of the additive characteristic times as a kinetic model, which gives poor results when reversible reactions are present and there is temperature gradient inside the pellet. Based on these, Niksiar and Rahimi (13) developed a one-dimensional (in the *z* direction) transient model where gas and solid streams are assumed to be in plug flow condition. This model is based on the grain model as kinetic model instead of the law of additive characteristic times used in Dussoubs et al. (10), in which the pellets are composed of spherical nonporous grains with uniform initial radius, and the reactions take place at the unreacted core of the grains. Another difference is that it neglects the calcination reaction, since a study from the authors revealed that the rate expression and its coefficients over predict the reaction rate (14). In order to validate their model, the authors used the same operating parameters from Dussoubs et al. (10, 12) and compared the trends of the measured and the calculated data from the same article through the reactor length. Additionally, the model verifies the effects of increasing solid feed temperature and inlet HF flow in the horizontal zone. For the former, it was found that UF_4 fraction in the products remain largely unchanged, and, for the latter, it was found that UF_4 fraction is greatly diminished in the product stream, which is a similar conclusion from (12).

Finally, Bykov et al. (15) proposed a “shrinking core” model, based on the studies by Dussoubs et al (10, 12), for obtaining the radius of the unreacted part of the solid granule (thus, reaction conversion) along the vertical hydrofluorination zone through a period of time. According to the article, the use of this model is justified because the entire process is limited by diffusion of the gaseous compounds through the layer of ashes from the burnt uranium compound, and it is possible to ignore the rate of counter reaction because it occurs in the temperature range lower than the point of Gibbs energy sign inversion. The article also

includes a thermodynamic assessment to justify changes for the expression of the thermodynamic equilibrium constant.

3.2. OTHER MODELS FOR GAS-SOLID MOVING BED REACTORS

Supported by their findings in (13), Niksiar and Rahimi (16) expanded their model in order to make it generic for a moving-bed reactor encompassing any number of non-catalytic gas-solid reactions (reversible or not). This model includes non-steady mass and energy balances for both phases in the axial direction, using the grain model as kinetic model and the degree of reaction progress as a parameter for each reaction. The model is then validated by comparing the results of the direct reduction of the iron oxide pellets using a H_2 and CO mixture with those obtained experimentally by Takenaka et al. (17). Many correlations, such as the effective thermal conductivity of the pellet and the heat transfer coefficients, can also be used in the UF_4 production model.

Niksiar and Rahimi (18) further applied the shrinking core model as the kinetic model for the reduction of hematite, and arrived at the following major conclusions:

1) both models are appropriate, and exhibit similar results, only if the reaction is relatively fast (that is, the reaction is controlled by diffusion) and the pellets are relatively large; and
2) the increase in the pellet porosity produces a significant difference in the results, with the shrinking core model resulting in larger errors, which can be observed for pellet porosities as low as 0.25.

Valipour and Saboohi (19) also presented a generic model for multiple gas-solid reactions in porous pellets, which was validated by comparing results with experimental data, both for microscopic (single pellet) and macroscopic (counter current moving bed reactor) scales. In this particular article, experiments from the controlled hematite reduction in Usui et al. (20) and Takenaka et al. (17) were used as data. A review of the previous investigations on these kinds of reactions is also provided, as well as diverse correlations for the physico-chemical properties. However, no sensitivity analysis was made for the model parameters.

Although there are some references in literature related to the modeling of the vertical module due to its simple geometry (cylindrical), the same cannot be stated for the horizontal hydroflorination zone, due to the presence of the screw, which dramatically increases

geometry complexity, and thus, computational resources. In order to solve this issue, Poulesquen and Vernes (21) and Kumar et al. (22) proposed to use a series of CSTRs to simulate the empty spaces between the blades of a co-rotating twin-screw extruder, which is a similar approach to the one used by Dussoubs et al. to model the horizontal module (10). A more recent study by Shi et al. (23, 24) proposed a non-steady state model for the slow pyrolysis of char in a single screw reactor using 3D CFD analysis.

3.3. CHEMICAL REACTIONS

As stated in the previous sections, a total of six chemical reactions occur in the furnace. Dussoubs et al. (10) reported kinetic data, such as heat of reaction and rate expression for each reaction, with the law of additive reaction times proposed by Sohn (25) being used for the reduction and hydrofluorination reactions.

More detailed expressions of the characteristic times can be found in specific application of this kinetic model for the case of the moving bed furnace treated in the work by Patisson et al. (26). However, neither of these references provide kinetic information, such as the Arrenhius pre-exponential factor, used in the kinetic model proposed by Sohn (25).

The cracking of ammonia is a widely known process due to the fact that anhydrous ammonia is an excellent storage medium for hydrogen, offering advantages in cost and convenience as a fuel, such as the possibility to produce H_2 on-site or on-board with simple start-up procedures and low weight equipment (27). There are several studies regarding the kinetic of this reaction with the use of specific catalysts, among which, Itoh et al. (2002) (28) present a fine powder of Fe-MO_x and, more recently, Polanski et al. (29) introduced Pd nanoparticles supported by Ni. Still, since the cracking reaction inside the moving bed reactor occurs without these catalysts, no kinetic data can be utilized from these works.

Although there are studies in the literature regarding the calcination reaction, for instance, the ones by Eloirdi et. al (30) and Manna et al. (31), they are limited to provide only information regarding X-ray diffraction and SEM analysis, respectively, and do not provide kinetic data. These studies, nevertheless, are important to provide the information that this reaction does occur in a temperature range that exists inside the furnace (450 ºC to 550 ºC), corroborating the assumption of neglecting this reaction made by Niksiar and Rahimi (13) in their model.

There are many studies regarding the reduction reactions using H_2 as reduction agent. While some articles include the study of the reductions of UO_3 and U_3O_8 as a single (in series) reaction, such as Dell and Wheeler (32), Heiskala (33), Le Page and Fane (34), and Alfaro et al. (35), others, such as Pijolat et al. (36) and Sidorov and Sofronov (37), focus on the conversion of U_3O_8 to UO_2 (second part). Alternatively, the reduction of U_3O_8 to UO_2 directly with ammonia was studied by Valdivieso et al. (38) using mass spectrometry, which concluded that the ammonia decomposition occurs at about 700ºC only in the presence of UO_2, that acts as a catalyst. Finally, Notz and Mendel (39), aided by X-ray analysis, also provided kinetic data and a reaction mechanism for these reactions.

Contrary to the other reactions, the hydrofluorination lacks recent findings in the literature, being its newest development described by Nicole et al. (40), which also provides expression for the characteristic times for this reaction. Tomlinson et al. (41) and Costa and Smith (42) also provide information regarding this topic, although it must be noted that the temperatures used in their experiments were low to medium, which is outside the range typically present in the modules of the furnace of this work.

4. METHODS AND MODEL

Although the model proposed by Niksiar and Rahimi (13) is more recent and covers certain drawbacks contained in the model proposed by Dussoubs et al. (10), it brings about new disadvantages, such as the consideration that the calcination reaction does not occur, which was disproven by Eloirdi et al. (30) and Manna et al. (31) as discussed in the literature review, and the contemplation that all variables only change in the axial direction (*z* coordinate), which was disproven by the results in Dussoubs et al. (10), that showed that the temperature and reaction rates changes depend on the radial position (*r* coordinate). Thus, the model presented in the latter will be used as base for the vertical zones in this work. Since the horizontal zone is modeled as a series of CSTRs in both references, the model used by Niksiar and Rahimi (13) will be adopted, with some modifications. Unless specified otherwise, all values have the same units as described in the "List of Abbreviations and Symbols" section.

The general premises used in this work are the same used in the references which the data were extracted from, and are summarized as follows. Premises pertaining specifically to this work are also described in this item.

1) Solid flow is considered piston type without dispersion, while gas flow is also assumed as piston type, but with dispersion in radial and axial directions. Solid drag was not considered for the model;
2) The moving bed is considered as a cubic stack of non-overlapping impermeable spherical pellets, randomly distributed, of mean diameter d_p, forming a porous medium (bed) with porosity ε_b. Although these values remain constant within a zone, they may change from one zone to another;
3) The moving bed is considered a pseudo-homogeneous medium, thus, gas and solid temperatures are considered equal. This premise is only applicable to calculations performed in the vertical section;
4) Conductive and convective heat transfer, as well as transfer by radiation, will be considered in the model;
5) The gaseous compounds, as well as the gaseous phase as a whole, will be modeled as ideal gases. This assumption is valid, since, although some components present a strong chemical intramolecular force, they are all submitted to atmospheric pressure;

6) Since the model considers steady state flow, all derivatives related to time are zero ($\partial/\partial t = 0$);
7) The symmetrical (cylinder) geometry implies that all azimuthal derivatives are zero ($\partial/\partial\theta = 0$);
8) Only the *z* component of the velocity vector will be considered. In other words, $u_r = u_\theta = 0$;
9) The momentum balance will be modeled using Egrun's Law; and
10) An average value for solid and gaseous phase compositions will be considered for each zone (with the Horizontal Hydrofluorination zone being an exception), according to the following items:
    a) Reduction zone: 100 wt% UO_2 (solid phase); 80 mol% H_2O and 20 mol% N_2 (gas phase), justified by the rapid kinetic reactions that occur in this zone;
    b) Buffer zone: 100 wt% UO_2 (solid phase); 95 mol% H_2O and 5 mol% HF (gas phase); and
    c) Vertical Hydrofluorination zone: 50 wt% UO_2 and 50 wt% UF_4 (solid phase); 95 mol% H_2O and 5 mol% HF (gas phase).

4.1. MODEL CONSTANTS

The constant values used for some parameters in the model of this work can be divided in two main groups: some are global constants for the whole geometry of the model, while others are constant within a zone. These values are summarized in **Table 2** and **Table 3**. Values that do not have a reference were premised for this work.

Table 2 – Constants used in the model – applicable to all zones.

Constant	Value	Ref.	Constant	Value	Ref.	Constant	Value	Ref.
$\mathbf{R}$	8.314	(43)	$\boldsymbol{\varepsilon_t}$	$9.0*10^{-1}$	(44)	$\mathbf{Cp_{U3O8}}$	$1.160*10^{2}$	(45)
$\mathbf{M_{UO3}}$	$2.863*10^{-1}$	(43)	$\mathbf{h_{ext}}$	$2.5*10^{1}$	(46)	$\mathbf{Cp_{UO2F2}}$	$1.080*10^{3}$	(47)
$\mathbf{M_{UO2}}$	$2.700*10^{-1}$	(43)	$\mathbf{T_{ext}}$	300	-	$\mathbf{Cp_{UF4}}$	$1.269*10^{2}$	(48)
$\mathbf{M_{U3O8}}$	$8.421*10^{-1}$	(43)	$\mathbf{T_0}$	298	(13)	$\boldsymbol{\lambda_{UF4}}$	$2.4*10^{-1}$	(49)
$\mathbf{M_{UO2F2}}$	$3.080*10^{-1}$	(43)	$\mathbf{T_{aq}}$	800	-	$\mathbf{u_s}$	$-2.0*10^{-4}$	(1)
$\mathbf{M_{UF4}}$	$3.140*10^{-1}$	(43)	$\mathbf{Cp_{UO3}}$	$3.420*10^{2}$	(50)	$\mathbf{u_g}$	$6.0*10^{-1}$	(10)
$\boldsymbol{\varepsilon_p}$	$5.0*10^{-1}$	(12)	$\mathbf{Cp_{UO2}}$	$3.150*10^{2}$	(50)			

(1) Mass flow of approximately 20 kg/h considered as calculation basis. Value is taken negative, since solids flow is contrary to *z* axis.

Table 3 – Constants used in the model – applicable to specific zones.

Constant	Application	Value
$\mathbf{d_p}$	Reduction Zone	$2.5*10^{-2}$
	Buffer Zone	
	Vertical Hydrofluorination Zone	$6.0*10^{-3}$
	Horizontal Hydrofluorination Zone	
$\boldsymbol{\varepsilon_b}$	Reduction Zone	
	Buffer Zone	$5.0*10^{-1}$
	Vertical Hydrofluorination Zone	
	Horizontal Hydrofluorination Zone	$4.0*10^{-1}$

Source: (10).

4.2. BALANCE EQUATIONS

The balance equations proposed by Dussoubs et al. (10) and used in this work to model the vertical section are summarized **Table 4** and **Table 5**, with some adaptations. The variables that are results of solving each equation are displayed between parenthesis in the "Description" column.

In order to reduce the number of variables, the product of total concentration and weight or molar fraction was condensed into species molar or weight concentration. This was not done in Dussoubs et al. (10) because it was needed for the linearization step of the Gauss-Seidel method for solving a system of PDEs. In this work, the solving method is the one used by MATLAB® (Newton method). So, this simplification is not detrimental.

As indicated in the previous paragraph, the balance equations constitute a system of PDEs, which must be solved numerically, since the reaction rates depend on reactant concentrations, which vary along the reactor.

Table 4 - Balance Equations for the vertical section of the furnace – Reduction and Intermediate Zones.

Description	Equation	Num.
Matter balance for solid phase (ρ_t)	$\mathbf{u_s}\frac{\partial \rho_t}{\partial z} = (M_{U3O8} - 3M_{UO3})r_{red1} + (3M_{UO2} - M_{U3O8})r_{red2} + (M_{UO2F2} - M_{UO3})r_{hfs}$	(1)
Matter balance for UO_3 (ρ_{UO3})	$\mathbf{u_s}\frac{\partial \rho_{UO3}}{\partial z} = -M_{UO3}(3r_{red1} + r_{hfs})$	(2)
Matter balance for UO_2 (ρ_{UO2})	$\mathbf{u_s}\frac{\partial \rho_{UO2}}{\partial z} = 3M_{UO2}r_{red2}$	(3)
Matter balance for U_3O_8 (ρ_{U3O8})	$\mathbf{u_s}\frac{\partial \rho_{U3O8}}{\partial z} = M_{U3O8}(r_{red1} - r_{red2})$	(4)
Matter balance for UO_2F_2 (ρ_{UO2F2})	$\mathbf{u_s}\frac{\partial \rho_{UO2F2}}{\partial z} = M_{UO2F2}r_{hfs}$	(5)
Matter balance for UF_4 (ρ_{UF4})	$\mathbf{u_s}\frac{\partial \rho_{UF4}}{\partial z} = 0$	(6)
Matter balance for gas phase (c_t)	$\mathbf{u_g}\frac{\partial c_t}{\partial z} = 2r_{cr} - r_{hfs}$	(7)
Matter balance for NH_3 (c_{NH3})	$\mathbf{u_g}\frac{\partial c_{NH3}}{\partial z} = -2r_{cr} + [\frac{\mathbf{D_r}}{r}\frac{\partial}{\partial r}\left(r\frac{\partial c_{NH3}}{\partial r}\right) + \mathbf{D_z}\frac{\partial}{\partial z}\left(\frac{\partial c_{NH3}}{\partial z}\right)]$	(8)
Matter balance for N_2 (c_{N2})	$\mathbf{u_g}\frac{\partial c_{N2}}{\partial z} = r_{cr} + [\frac{\mathbf{D_r}}{r}\frac{\partial}{\partial r}\left(r\frac{\partial c_{N2}}{\partial r}\right) + \frac{\partial}{\partial z}\left(\frac{\partial c_{N2}}{\partial z}\right)]$	(9)
Matter balance for H_2 (c_{H2})	$\mathbf{u_g}\frac{\partial c_{H2}}{\partial z} = 3r_{cr} - r_{red1} - 2r_{red2} + [\frac{\mathbf{D_r}}{r}\frac{\partial}{\partial r}\left(r\frac{\partial c_{H2}}{\partial r}\right) + \mathbf{D_z}\frac{\partial}{\partial z}\left(\frac{\partial c_{H2}}{\partial z}\right)]$	(10)
Matter balance for H_2O (c_{H2O})	$\mathbf{u_g}\frac{\partial c_{H2O}}{\partial z} = r_{red1} + 2r_{red2} + r_{hfs} + [\frac{\mathbf{D_r}}{r}\frac{\partial}{\partial r}\left(r\frac{\partial c_{H2O}}{\partial r}\right) + \mathbf{D_z}\frac{\partial}{\partial z}\left(\frac{\partial c_{H2O}}{\partial z}\right)]$	(11)
Matter balance for HF (c_{HF})	$\mathbf{u_g}\frac{\partial c_{HF}}{\partial z} = -2r_{hfs} + [\frac{\mathbf{D_r}}{r}\frac{\partial}{\partial r}\left(r\frac{\partial c_{HF}}{\partial r}\right) + \mathbf{D_z}\frac{\partial}{\partial z}\left(\frac{\partial c_{HF}}{\partial z}\right)]$	(12)
Heat balance for the bed (T)	$(\mathbf{u_s}\rho_t\mathbf{C_{p,s}} + \mathbf{u_g}c_t\mathbf{C_{p,g}})\frac{\partial T}{\partial z} = -\sum_j \Delta H_{r,j}r_j + \boldsymbol{\lambda_{eff}}[\frac{1}{r}\frac{\partial}{\partial r}\left(r\frac{\partial T}{\partial r}\right) + \frac{\partial}{\partial z}\left(\frac{\partial T}{\partial z}\right)]$	(13)
Momentum balance (p)	$-\frac{\partial p}{\partial z} = 150\frac{(1-\varepsilon_b)^2}{\varepsilon_b^3 d_p^2}\boldsymbol{\mu_g}\mathbf{u_g} + 1.75\frac{1-\varepsilon_b}{\varepsilon_b^3 d_p}\boldsymbol{\rho_g}\mathbf{u_g}^2$	(14)

Source: Adapted from (10).

Table 5 - Balance Equations for the vertical section of the furnace – Vertical Hydrofluorination Zone.

Description	Equation	Num.
Matter balance for solid phase (ρ_t)	$\mathbf{u_s}\frac{\partial \rho_t}{\partial z} = (M_{UF4} - M_{UO2})r_{hf}$	(15)
Matter balance for UO_2 (ρ_{UO2})	$\mathbf{u_s}\frac{\partial \rho_{UO2}}{\partial z} = -M_{UO2}r_{hf}$	(16)
Matter balance for UF_4 (ρ_{UF4})	$\mathbf{u_s}\frac{\partial \rho_{UF4}}{\partial z} = M_{UF4}r_{hf}$	(17)
Matter balance for gas phase (c_t)	$\mathbf{u_g}\frac{\partial c_t}{\partial z} = -2r_{hf}$	(18)
Matter balance for H_2O (c_{H2O})	$\mathbf{u_g}\frac{\partial c_{H2O}}{\partial z} = 2r_{hf} + [\frac{\mathbf{D_r}}{r}\frac{\partial}{\partial r}\left(r\frac{\partial c_{H2O}}{\partial r}\right) + \mathbf{D_z}\frac{\partial}{\partial z}\left(\frac{\partial c_{H2O}}{\partial z}\right)]$	(19)
Matter balance for HF (c_{HF})	$\mathbf{u_g}\frac{\partial c_{HF}}{\partial z} = -4r_{hf} + [\frac{\mathbf{D_r}}{r}\frac{\partial}{\partial r}\left(r\frac{\partial c_{HF}}{\partial r}\right) + \mathbf{D_z}\frac{\partial}{\partial z}\left(\frac{\partial c_{HF}}{\partial z}\right)]$	(20)
Heat balance for the bed (T)	$(\mathbf{u_s}\rho_t\mathbf{C_{p,s}} + \mathbf{u_g}c_t\mathbf{C_{p,g}})\frac{\partial T}{\partial z} = -\Delta H_{r,hf}r_{hf} + \boldsymbol{\lambda_{eff}}[\frac{1}{r}\frac{\partial}{\partial r}\left(r\frac{\partial T}{\partial r}\right) + \frac{\partial}{\partial z}\left(\frac{\partial T}{\partial z}\right)]$	(21)
Momentum balance (p)	$-\frac{\partial p}{\partial z} = 150\frac{(1-\varepsilon_b)^2}{\varepsilon_b^3 d_p^2}\boldsymbol{\mu_g}\mathbf{u_g} + 1.75\frac{1-\varepsilon_b}{\varepsilon_b^3 d_p}\boldsymbol{\rho_g}\mathbf{u_g}^2$	(22)

Source: Adapted from (10).

For the horizontal section, the equations proposed by Niksiar and Rahimi (13) were used, with some alterations, once the article considers the grain model as kinetic model, which is not done in this work. Thus, in order to account for a "broader" scope, some terms were replaced for more macroscopic parameters, such as reactor volume and bed porosity. Also, since this section is modeled as a series of CSTRs, the matter and energy balances need to be performed for each individual reactor. It should also be noted that two heat balances (one for each phase) are performed per CSTR, since the premise of pseudo-homogeneous medium is no longer valid due to the solid phase being concentrated at the "floor" of the horizontal section, instead of being dispersed in its entire volume.

Unlike the vertical section, the balance equations of the horizontal zone comprise a system of nonlinear equations, which can be solved using Newton method or similar, such as the Trust-Region-Dogleg algorithm (based on Powell's dog leg method) used in MATLAB®. These equations are summarized in **Table 6**.

Table 6 - Balance Equations for the horizontal section of the furnace.

Num.	Description	Equation
(23)	Matter balance for H_2O ($F_{H2O}(n)$)	$F_{H2O}(n-1) - F_{H2O}(n) + 2r_{hf}(n)\mathbf{V_{CSTR}} = 0$
(24)	Matter balance for HF ($F_{HF}(n)$)	$F_{HF}(n-1) - F_{HF}(n) - 4r_{hf}(n)\mathbf{V_{CSTR}} = 0$
(25)	Matter balance for UO_2 ($F_{UO2}(n)$)	$F_{UO2}(n-1) - F_{UO2}(n) - r_{hf}(n)\mathbf{V_{CSTR}} = 0$
(26)	Matter balance for UF_4 ($F_{UF4}(n)$)	$F_{UF4}(n-1) - F_{UF4}(n) + r_{hf}(n)\mathbf{V_{CSTR}} = 0$
(27)	Heat balance, gas phase ($T_g(n)$)	$[F_{H2O}(n) + F_{HF}(n)]Cp_g(n)[T_g(n) - \mathbf{T_0}] - [F_{H2O}(n-1) + F_{HF}(n-1)]Cp_g(n-1)[T_g(n-1) - \mathbf{T_0}] - U(n)\mathbf{A_{CSTR}}[T_g(n) - T_{aq}] - \Delta H_{hf}(n)r_{hf}(n)\mathbf{V_{CSTR}} - h(n)[1 - \boldsymbol{\varepsilon_b}]\mathbf{A_{CSTR}}[T_s(n) - T_g(n)] = 0$
(28)	Heat balance, solid phase ($T_s(n)$)	$[F_{UO2}(n) + F_{UF4}(n)]Cp_s(n)[T_s(n) - \mathbf{T_0}] - [F_{UO2}(n+1) + F_{UF4}(n+1)]Cp_s(n+1)[T_s(n+1) - \mathbf{T_0}] - U(n)\mathbf{A_{CSTR}}[T_s(n) - \mathbf{T_{aq}}] - \Delta H_{hf}(n)r_{hf}(n)\mathbf{V_{CSTR}} - h(n)[1 - \boldsymbol{\varepsilon_b}]\mathbf{A_{CSTR}}[T_s(n) - T_g(n)] = 0$

Source: Adapted from (13).

4.3. GOVERNING EQUATIONS

In order to complement the balance equations, other equations are needed to find the appropriate values of the variables, such as heat capacity of each phase and effective thermal conductivity, as well as kinetic rate expressions. Since they depend on model variables (mainly temperature), the governing equations must be provided to calculate them. This item is dedicated to describing such equations, and is divided into three topics: material and transport parameters, kinetic parameters, and, finally, the equations describing the initial concentrations for ammonia, hydrogen and nitrogen used in the reduction zone.

4.3.1 Material and transport parameters

In order to obtain results from the various equations and correlations described in this work, it is first necessary to present the information collected in the literature to describe properties which are intrinsic for each chemical compound, such as viscosity and heat capacity.

It should be noted that all governing equations are explicitly described for the vertical section of the furnace. In order to adjust them for the horizontal zone, one must interpret that, instead of varying with *r* and/or *z*, the variables depend on *n*. Also, the premise that the average composition remains constant throughout the whole zone is not applicable, and must be calculated for each CSTR reactor.

4.3.1.1 Gas densities

One of the parameters needed for dimensionless number correlations is the density of the gaseous phase, while the molecular weights of each compound appear in various equations and correlations throughout this work. In order to calculate it, first it is needed to calculate the density of each gaseous compound according to the ideal gas equation described in equation (29):

$$\rho_{i(\mathrm{gas})} = \frac{\mathbf{p_0 M_i}}{\mathbf{R}\mathrm{T}} \tag{29}$$

Thus, by including the average composition of the gaseous phase as stated in the premises, it is possible to obtain the average gas density in a given zone using the equation (30):

$$\rho_{\mathrm{g}} = \sum_{i} \mathbf{x}_{\boldsymbol{i}(\mathbf{gas})} \rho_{\mathrm{i(gas)}} \tag{30}$$

In order to validate the premise for the use of the ideal gas equation, the correlated density for the gaseous compounds of the model is summarized in **Table 7**, for the temperature of 748 K, which represents the average temperature inside the whole furnace. **Table 7** also includes the calculation of densities using the ideal gas equation.

Table 7 – Densities of gaseous compounds at T = 748 K.

Compound	Ideal Density	Real Density (43)	Diff. (%)
NH_3	$2.7379*10^{-1}$	$2.7289*10^{-1}$	0.3299
N_2	$4.5031*10^{-1}$	$4.5064*10^{-1}$	-0.0723
H_2	$3.2410*10^{-2}$	$3.1608*10^{-2}$	2.4761
H_2O	$2.8971*10^{-1}$	$2.9082*10^{-1}$	-0.3856
HF	$3.2154*10^{-1}$	-	-

The last column of **Table 7** shows the percent difference between density considering ideal gas model and experimental data, and, as seen, the hypothesis of ideal gas seems plausible. Another fact that reinforces this premise is the atmospheric pressure used in the furnace.

4.3.1.2 Gas viscosities

The dynamic viscosity of each fluid (gas) was predicted according to the correlations presented in Green et al. (43), obtaining the results presented in **Table 8**.

Table 8 – Correlations used for gas viscosities in the furnace.

Compound	Correlation	Num.
N_2	$\frac{6.5592 * 10^{-7} T^{0.6081}}{1 + 54.71/T}$	(31)
H_2O	$1.7096 * 10^{-8} T^{1.1146}$	(32)
HF	$\frac{4.5101 * 10^{-14} T^{3.005}}{1 - 521.83/T + 76.111/T^2}$	(33)

Source: (43).

* Since the viscosities for the other gaseous compounds were not needed in the model, their correlations were omitted.

The average gas viscosity is also needed for some equations. In order to obtain this information, one must consider the gas composition in each reactor location. However, this would bring about a great increase in the problem complexity, so, to circumvent excessive

computation times, an assumption was made to keep this value remains constant throughout the zones. In order to calculate the viscosity of the gaseous phase, the correlation proposed by Wilke (51) for a binary mixture was used:

$$\mu_g = \frac{\mu_1}{1 + \frac{\frac{\mathbf{x_2}}{\mathbf{x_1}}\left[1 + \left(\frac{\mu_1}{\mu_2}\right)^{0.5}\left(\frac{\mathbf{M_2}}{\mathbf{M_1}}\right)^{0.25}\right]^2}{\frac{4}{\sqrt{2}}\left[1 + \left(\frac{\mathbf{M_2}}{\mathbf{M_1}}\right)\right]^{0.5}}} + \frac{\mu_2}{1 + \frac{\frac{\mathbf{x_1}}{\mathbf{x_2}}\left[1 + \left(\frac{\mu_2}{\mu_1}\right)^{0.5}\left(\frac{\mathbf{M_1}}{\mathbf{M_2}}\right)^{0.25}\right]^2}{\frac{4}{\sqrt{2}}\left[1 + \left(\frac{\mathbf{M_1}}{\mathbf{M_2}}\right)\right]^{0.5}}} \quad (34)$$

4.3.1.3 Reynolds Number

The dimensionless Reynolds number is useful for predicting flow patterns in different situations. In the case of packed beds, it is expressed by the formula described in Dwivedi and Upadhyay (52), which uses the particle (pellet) diameter as characteristic length:

$$\mathrm{Re} = \frac{\rho_g \mathbf{u_g}}{\mu_g} * \mathbf{d_p} \quad (35)$$

It should be stated that the pellet diameter was also used as characteristic length in other dimensionless numbers, such as the Nusselt number.

4.3.1.4 Heat Capacities for gases

One of the variables in the convective term of the heat balance provided in the article by Dussoubs et al. (10) is the heat capacity of each phase. In order to obtain these values, an investigation in the literature was performed, obtaining the values presented in **Table 9**. It should be noted that the heat capacity for solid compounds was already provided in the Model Constants section.

Table 9 – Correlations for specific heats used in the model.

Compound	Correlation	Num.
NH_3	$4.184(6.7 + 6.3 * 10^{-2}\mathrm{T})$	(36)
N_2	$4.184(6.5 + 10^{-3}\mathrm{T})$	(37)
H_2	$4.184(6.62 + 8.1 * 10^{-4}\mathrm{T})$	(38)
H_2O	$4.184(8.22 + 1.5 * 10^{-4}\mathrm{T} + 1.34 * 10^{-6}\mathrm{T}^2)$	(39)
HF	$30.117 - (3.247 * 10^{-3}\mathrm{T} + 2.87 * 10^{-6}\mathrm{T}^2 + 4.58 * 10^{-10}\mathrm{T}^3)$	(40)

Source: (43).

With this information, it is possible to calculate the average property for each phase according to the equations (41) and (42):

$$\mathrm{C_{p,s}} = \sum_i \mathbf{w_{\boldsymbol{i}(solid)}} \mathbf{C_{p,\boldsymbol{i}(solid)}} \tag{41}$$

$$\mathrm{C_{p,g}} = \sum_i \mathbf{x_{\boldsymbol{i}(gas)}} \mathrm{C_{p,\boldsymbol{i}(gas)}} \tag{42}$$

4.3.1.5 Thermal conductivities

The effective thermal conductivity will be the proportionality constant used in the conductive side of the fluid bed heat balance, however, in order to find it, the thermal conductivity of each compound must be known. **Table 10** summarizes the correlations used to calculate these values. It should be noted that the thermal conductivity for UF_4 was given in the Model Constants section, and, if the correlation of a component was not described in the aforementioned Table, it means it was not needed for the calculations, being, therefore, omitted.

Table 10 – Correlations for thermal conductivities used in the model.

Phase	Compound	Correlation	Ref.	Num.
Solid	UO_2	$\frac{115.8}{7.54 + 1.77 * 10^{-2}T + 3.61 * 10^{-6}T^2}$	(53)	(43)
Gaseous	N_2	$\frac{3.31 * 10^{-4}T^{0.7722}}{1 + \frac{16.32}{T} + \frac{373.72}{T^2}}$	(43)	(44)
	H_2O	$6.2 * 10^{-6}\mathrm{T}^{1.3973}$	(43)	(45)
	HF	$\frac{3.46 * 10^{-5}T^{1.1224}}{1 + \frac{18.744}{T}}$	(43)	(46)

In order to calculate the average thermal conductivity for each phase, the following expressions used by Valipour (54) were used:

$$\lambda_{\mathrm{s}} = \sum_i \mathbf{w}_{i(\mathbf{solid})}\lambda_{i(\mathrm{solid})} \tag{47}$$

$$\lambda_{\mathrm{g}} = \sum_i \mathbf{x}_{i(\mathbf{gas})}\lambda_{i(\mathrm{gas})} \tag{48}$$

Finally, the expression for the effective thermal conductivity is the same used in Valipour and Saboohi (19), and transcribed in equations (49) to (51):

$$\lambda_{\mathrm{eff\,(conductive)}} = \frac{1}{3}\{(1-\boldsymbol{\varepsilon}_{\mathbf{p}})\lambda_{\mathrm{s}} + \boldsymbol{\varepsilon}_{\mathbf{p}}\lambda_{\mathrm{g}}\} + \frac{2}{3}\{\frac{(1-\boldsymbol{\varepsilon}_{\mathbf{p}})}{\lambda_{\mathrm{s}}} + \boldsymbol{\varepsilon}_{\mathbf{p}}\lambda_{\mathrm{g}}\}^{-1} \tag{49}$$

$$\lambda_{\mathrm{eff\,(radiative)}} = \frac{1-\boldsymbol{\varepsilon}_{\mathbf{p}}}{\frac{1}{\lambda_{\mathrm{s}}} + \frac{1}{0.691\boldsymbol{\varepsilon}_{\mathbf{t}}\mathbf{d}_{\mathbf{p}}(\frac{\mathrm{T}^3}{10^8})}} + 0.691\boldsymbol{\varepsilon}_{\mathbf{p}}\boldsymbol{\varepsilon}_{\mathbf{t}}\mathbf{d}_{\mathbf{p}}(\frac{\mathrm{T}^3}{10^8}) \tag{50}$$

$$\lambda_{\mathrm{eff}} = \lambda_{\mathrm{eff\,(conductive)}} + \lambda_{\mathrm{eff\,(radiative)}} \tag{51}$$

4.3.1.6 Heat transfer coefficients

For calculations in the vertical section, the convective heat transfer coefficient is mainly needed to specify the boundary conditions for temperature, in cases where there is no muffle in the walls. It is obtained by combining the definition of the Nusselt number with the empirical relation described in Niksiar and Rahimi (13), summarized in equation (52):

$$\mathrm{Nu} = \frac{\mathrm{h}\mathbf{d_p}}{\lambda_g} \rightarrow \mathrm{h} = \frac{\lambda_g}{\mathbf{d_p}}(2 + 0.39\mathrm{Re}^{0.5}\mathrm{Pr}^{0.33}) \tag{52}$$

For the horizontal section, a radiation component is also added to equation (52), generating equation (53), also described in Niksiar and Rahimi (13):

$$\mathrm{h} = \frac{\lambda_g}{\mathbf{d_p}}(2 + 0.39\mathrm{Re}^{0.5}\mathrm{Pr}^{0.33}) + 5.67 * 10^{-8}\boldsymbol{\varepsilon_t}\left(\mathrm{T_g} + \mathrm{T_s}\right)\left(\mathrm{T_g^2} + \mathrm{T_s^2}\right) \tag{53}$$

The overall heat transfer coefficient, used in the energy balance of the horizontal zone, is also obtained by the correlation described in Niksiar and Rahimi (13), and shown in equation (54):

$$\mathrm{U} = \frac{\mu_g}{\mathbf{d_p}}(2.26\mathrm{Re}^{0.8}\mathrm{Pr}^{0.33})\exp(-\frac{\mathbf{d_p}}{2\mathbf{R_0}}) \tag{54}$$

4.3.1.7 Dispersion Coefficients

Mass transfer parameters are used in the balance equations. More specifically, axial (longitudinal) and radial (transversal) dispersion coefficients are used in the matter balances for components in the gaseous phase, and are obtained using correlations with dimensionless numbers described herein. Instead of using the correlations present in Dussoubs et al. (10), this work utilizes more recent correlations for the calculation of the dispersion coefficients, namely the ones presented in Foumeny et al. (55) for steady state flow, described in equations (55) and (56):

$$\frac{1}{\mathrm{Pe_r}} = \frac{\mathrm{D}_r}{\mathbf{u_g d_P}} \rightarrow \mathrm{D}_r = \left[\frac{0.34}{(\mathrm{Re.\,Sc})^{0.8}} + \frac{0.08}{1 + \frac{10.8}{\mathrm{Re.\,Sc}}}\right]\mathbf{u_g d_P} \tag{55}$$

$$\frac{1}{\mathrm{Pe}_z} = \frac{\mathrm{D}_z}{\mathbf{u_g d_P}} \rightarrow \mathrm{D}_z = \left[\frac{0.72}{\boldsymbol{\varepsilon_b}\mathrm{Re.\,Sc}} + \frac{0.52}{1 + \frac{9}{\varepsilon_\mathrm{b}\mathrm{Re.\,Sc}}}\right]\mathbf{u_g d_P} \tag{56}$$

In order to calculate the Schmidt number used in the equations (55) and (56), the Fuller-Schettler-Giddings equation (for binary mixtures at 1 atm) is used for the diffusivity, resulting in the equation (57):

$$\mathrm{Sc} = \frac{\mu_\mathrm{g}}{\rho_\mathrm{g}} * \left[\frac{10^{-3}\mathrm{T}^{1.75}\left(\sum_\mathrm{i}\frac{1}{\mathbf{M}_i}\right)^{0.5}}{\left(\sum_i \frac{1}{\mathbf{V}_i}\right)^{1/3}}\right]^{-1} \tag{57}$$

4.3.2 Rate expressions and reaction kinetics

As stated previously in this work, a total of six reactions must be considered for the furnace. The calcination reaction is not be considered because, although its occurrence is known, there is no reliable data in the literature, since the values presented in Dussoubs et al. (10) were disputed by Niksiar and Rahimi (14). **Table 11** and **Table 12** present kinetic information regarding the reactions considered in the model.

Table 11 – Kinetic information for the reactions in the reduction + buffer zones.

Reaction	Heat of reaction @ 298 K	Activation energy	Pre-exponential factor	Ref.
Cracking $2NH_3 \rightarrow N_2 + 3H_2$	$1.611*10^5$	$1.611*10^5$	$8.4*10^8$ (s^{-1})	(10)
Reduction 1 $3UO_3 + H_2 \rightarrow U_3O_8 + H_2O$	$-1.5633*10^5$	$4.4*10^4$	$1.49*10^1$ (s^{-1})	(34)
Reduction 2 $U_3O_8 + 2H_2 \rightarrow 3UO_2 + 2H_2O$	$-1.6344*10^5$	$8.84*10^4$	$7.8*10^3$ (s^{-1})	(34)
Secondary Hydrofluorination $UO_3 + 2HF \rightarrow UO_2F_2 + H_2O$	$-1.1364*10^5$	$4.560*10^3$	$6.4*10^{-3}$ ($m^3.mol^{-1}.s^{-1}$)	(10)
Hydrofluorination $UO_2 + 4HF \leftrightarrow UF_4 + 2H_2O$	$-1.64*10^5$	$2.5*10^4$	$1.96*10^1$ (s^{-1})	(40)

Table 12 – Reaction rate expressions used in the model.

Reaction	Reaction rate (r_j, $mol.m^{-3}.s^{-1}$)	Ref.	Num.
Cracking $2NH_3 \rightarrow N_2 + 3H_2$	$r_{cr} = \mathbf{k_{0,cr}}\exp(-\frac{\mathbf{Ea_{cr}}}{\mathbf{R}T})c_{NH3}$	(10)	(58)
Reduction 1 $3UO_3 + H_2 \rightarrow U_3O_8 + H_2O$	$r_{red1} = \mathbf{k_{0,red1}}\exp(-\frac{\mathbf{Ea_{red1}}}{\mathbf{R}T})(\boldsymbol{y_{0,H2}})^{0.9}\rho_{UO3}(1-\boldsymbol{\varepsilon_b})$	(34)	(59)
Reduction 2 $U_3O_8 + 2H_2 \rightarrow 3UO_2 + 2H_2O$	$r_{red1} = \mathbf{k_{0,red2}}\exp(-\frac{\mathbf{Ea_{red2}}}{\mathbf{R}T})(\boldsymbol{y_{0,H2}})^{0.88}\rho_{U3O8}(1-\boldsymbol{\varepsilon_b})$	(34)	(60)
Secondary Hydrofluorination $UO_3 + 2HF \rightarrow UO_2F_2 + H_2O$	$r_{hfs} = \mathbf{k_{0,hfs}}\exp(-\frac{\mathbf{Ea_{hfs}}}{\mathbf{R}T})\rho_{UO3}(1-\boldsymbol{\varepsilon_b})c_{HF}$	(10)	(61)
Hydrofluorination $UO_2 + 4HF \leftrightarrow UF_4 + 2H_2O$	$r_{hf} = \mathbf{k_{0,hf}}\exp(-\frac{\mathbf{Ea_{hf}}}{\mathbf{R}T})\left(c_{HF} - \frac{\sqrt{c_{H2O}}}{K_{eq}}\right)$	(13)	(62)
	$K_{eq} = \left[\exp(\frac{224988}{\mathbf{R}T} - \frac{239.709}{\mathbf{R}})\right]^{0.25}\sqrt{\frac{\mathbf{R}T}{10^5}}$	(13)	(63)

(*) For the reduction 2 reaction, a value of N = 0 (reaction order in respect to solid reactant) was considered, since this is true for high temperatures (T > 650 ºC) (34), resulting in the expression described herein.

Equation (64) may be used for the heat of reaction given in the local temperature, since an average (constant) specific heat is used and all gases are treated as ideal.

$$\Delta H_{r,j} = \Delta \mathbf{H_{r,j}^{298}} + \Delta C_p(T - 298) \quad (64)$$

Using the information presented in **Table 13**, it is possible to obtain an expression for the heat of reaction in function of the bed temperature:

Table 13 – Heat of reaction in function of the bed temperature.

Reaction	ΔCp_j	Heat of reaction
Cracking	Cp_{N2} + 3* Cp_{H2}- 2* Cp_{NH3}	$1.611*10^5 + \Delta Cp_{cr}$ (T-298)
Reduction 1	$\mathbf{Cp_{U3O8}}$ + Cp_{H2O}- 3* $\mathbf{Cp_{UO3}}$ – Cp_{H2}	$-1.563*10^5 + \Delta Cp_{red1}$ (T-298)
Reduction 2	3* $\mathbf{Cp_{UO2}}$+ 2* Cp_{H2O}– $\mathbf{Cp_{U3O8}}$ – 2* Cp_{H2}	$-1.634*10^5 + \Delta Cp_{red2}$ (T-298)
Secondary Hydrofluorination	$\mathbf{Cp_{UO2F2}}$+ Cp_{H2O} – $\mathbf{Cp_{UO3}}$ – 2* Cp_{HF}	$-1.136*10^5 + \Delta Cp_{hfs}$ (T-298)
Hydrofluorination	$\mathbf{Cp_{UF4}}$ + 2* Cp_{H2O} – $\mathbf{Cp_{UO2}}$ – 4* Cp_{HF}	$-1.64*10^5 + \Delta Cp_{hf}$ (T-298)

4.3.3 Fraction of cracked ammonia in the feed

One of the parameters used in the model by Dussoubs et al. (10) is the fraction of ammonia, which is cracked due to pre-heating before entering the furnace. However, this value is not calculated, and is assumed by previous experience. In this model, this parameter is calculated depending on variables set by the operator, which can be easily measured or set, such as internal volume and temperature maintained in the muffle. For this end, the following premises are considered:

1) the muffle is considered as plug flow reactor (PFR) with constant and uniform temperature (T_{PFR} = 800 K);

2) ammonia is fed pure, at atmospheric pressure (1 atm) and ambient temperature ($T_{0,PFR}$ = 300 K);

3) pressure drop due to flow is considered negligible; and

4) ammonia is instantly heated to the final temperature inside the muffle as soon as it enters in the equipment.

A design equation for the case of an isothermal PFR with pure feed is provided by Fogler (56), which, adapted to the model in this work, becomes equation (65):

$$\frac{\mathbf{k_{0,cr}}\exp\left(-\frac{\mathbf{Ea_{cr}}}{\mathbf{R}\mathrm{T_{muf}}}\right)\mathbf{V_{muf}}}{\mathbf{\upsilon_{0,NH3,PFR}}\frac{\boldsymbol{T_{0,muf}}}{\boldsymbol{T_{muf}}}} + \boldsymbol{\delta_{cr}}\mathrm{X_{cr,muf}} + (\boldsymbol{\delta_{cr}}+1)\ln\left(\frac{1}{1-\mathrm{X_{cr,muf}}}\right) = 0 \qquad (65)$$

Thus, by solving this equation, the cracking conversion in the muffle ($X_{cr,muf}$) can be obtained, and the concentration of ammonia, hydrogen and nitrogen that enter in the furnace are given by equations (66) to (68):

$$\mathrm{c_{NH3,muf}} = \mathbf{c_{0,NH3,muf}}\frac{\left(1-\mathrm{X_{cr,muf}}\right)}{\left(1+\boldsymbol{\delta_{cr}}\mathrm{X_{cr,muf}}\right)}\frac{\mathbf{T_{0,muf}}}{\mathbf{T_{muf}}} \qquad (66)$$

$$\mathrm{c_{N2,muf}} = \mathbf{c_{0,NH3,muf}}\frac{0.5\left(\mathrm{X_{cr,muf}}\right)}{\left(1+\boldsymbol{\delta_{cr}}\mathrm{X_{cr,muf}}\right)}\frac{\mathbf{T_{0,muf}}}{\mathbf{T_{muf}}} \qquad (67)$$

$$\mathrm{c_{H2,PFR}} = \mathbf{c_{0,NH3,muf}}\frac{1.5\left(\mathrm{X_{cr,muf}}\right)}{\left(1+\boldsymbol{\delta_{cr}}\mathrm{X_{cr,muf}}\right)}\frac{\mathbf{T_{0,muf}}}{\mathbf{T_{muf}}} \qquad (68)$$

4.4. MODEL GEOMETRY

In order to obtain the results from all equations described herein, a suitable geometry that simulates the vertical section of furnace must be considered for solving the system of PDEs. Since the 3-D geometry for this section is symmetrical (cylinder), the problem was simplified to 2-D, originating the form in Figure **7**. The cylindrical coordinate system was adopted, with the axial origin (z coordinate) located at the bottom of the furnace, and the radial origin (r coordinate) located on the symmetry axis. It should be stated that, to facilitate comparison with data from the models existing in the literature, the results will be presented as a longitudinal "cut" of each vertical section of the furnace.

Figure 7 – Model geometry for the vertical section.

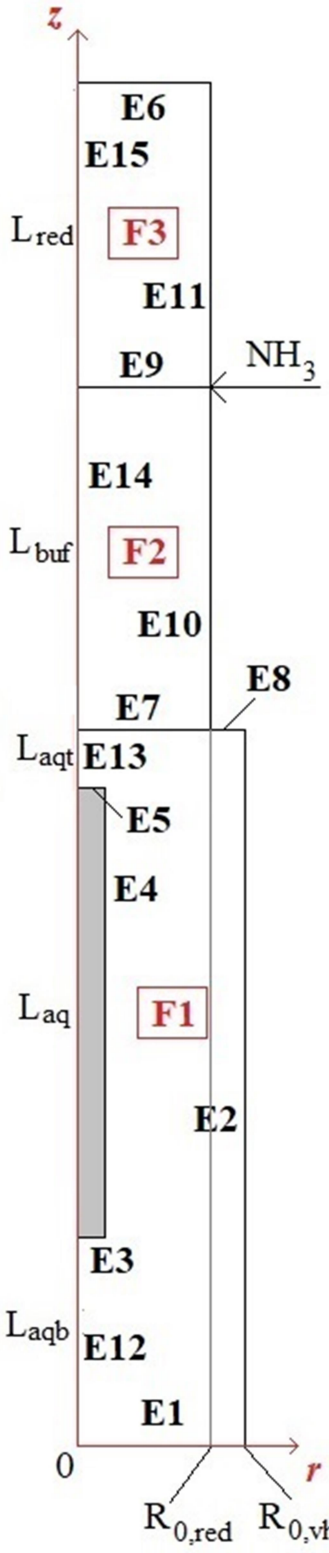

Note: Distances were omitted for confidentiality reasons. Figure is not at scale.

In MATLAB, the 2-D region is delimited by line segments known as “Edges” (E), while the region contained within these is called a “Face” (F). It is possible, the, to recreate

the 3-D model completely by assigning each of these elements the appropriate balance and governing equations and boundary conditions.

A more detailed description of each face and edge that forms the model geometry for the vertical section is presented below. Both elements are listed from the top of the equipment to its bottom, in order to make the text more understandable:

a) Faces:

• face (F3) represents the reduction zone;

• face (F2) represents the buffer zone; and

• face (F1) represents the vertical hydrofluorination zone. The grey area to the left represents the inside of the heat exchanger and, thus, is not part of the model geometry.

b) Edges:

• edge 6 (E6) constitutes the start of the reduction zone, and where the solids (UO3) are fed into the furnace and where the reduction gases exit the equipment;

• edge 11 (E11) depicts the wall that surrounds the reduction zone and is enveloped by a muffle;

• edge 9 (E9) represents the longitudinal end of the reduction zone (or the start of the buffer zone). For this work, cracked ammonia is also fed through this edge;

• edge 10 (E10) represents the wall that surrounds the buffer zone, and separates the interior of the furnace with the external environment (i.e., no muffle envelops this wall);

• edges 7 and 8 (E7 and E8, respectively) represent the longitudinal end of the reduction zone, and the start of the vertical hydrofluorination zone. It is also in this edge that a fraction of the gas is removed from the furnace. The existence of E8 (which is not connected to the buffer zone) is due to an increase in the diameter between these zones;

• edges 3, 4 and 5 (E3, E4 and E5, respectively) represent the wall that separates the interior of the vertical hydrofluorination zone with the heat exchanger;

• edge 2 (E2) represents the wall of the vertical hydrofluorination zone surrounded by the muffle;

• edge 1 (E1) represents the longitudinal end of the vertical hydrofluorination zone, and the start of the horizontal hydrofluorination zone; and

• edges 12, 13, 14 and 15 (E12, E13, E14 and E15, respectively) represent together the symmetry axis of the furnace.

Since the horizontal section is treated as a series of CSTRs, the geometry is different than in the vertical section. For that end, the latter section is divided in 14 CSTRs, each with the same volume and enveloped by a muffle, being modeled as oblique cylinders and better described by the dimensions in Figure **8**. It should be noted that the solid and gas entrances are not included in the model.

Figure 8 – Model geometry for the vertical section.

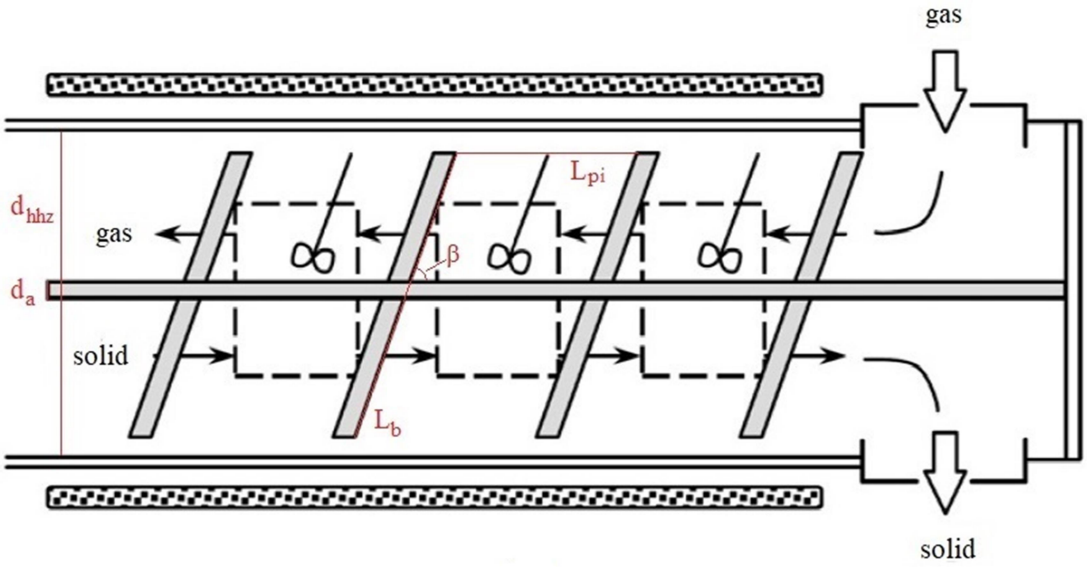

Source: Adapted from (13).

Note: Distances were omitted for confidentiality reasons. Figure is not at scale.

In order to calculate the volume used in the balance and governing equations described in this work, the equations (69) to (72) must be applied:

$$\boldsymbol{\beta} = \frac{\pi}{2} - \cos^{-1}\left(\frac{\mathbf{d_{hhz} - d_a}}{\mathbf{L_b}}\right) \tag{69}$$

$$\mathbf{L_{pi}} = \mathbf{L_b} * \sin\boldsymbol{\beta} \tag{70}$$

$$\mathbf{V_{CSTR}} = \pi * \left(\frac{\mathbf{d_{hhz}^2}}{4} - \frac{\mathbf{d_a^2}}{4}\right) * \mathbf{L_{pi}} \tag{71}$$

$$\mathbf{A_{CSTR}} = \pi \mathbf{d_{hhz} L_b} + \frac{\pi}{2}\mathbf{d_{hhz}^2} \tag{72}$$

Additionally, a more systematic view of the horizontal hydrofluorination zone as a series of CSTRs is shown in Figure **9**. The right side of the zone represents the gas entrance (and the solids exit), while the left side represents the solids entrance (and the gas exit). This figure also represents which variable is calculated in each reactor, and where the boundary conditions are applied.

Figure 9 – Systematic view of the horizontal section.

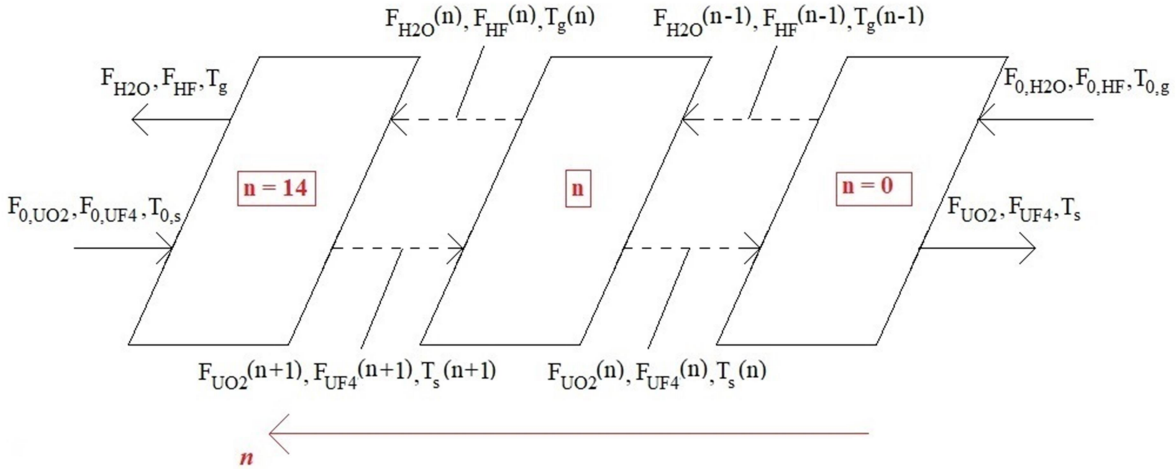

Note: Distances were omitted for confidentiality reasons. Figures are not at scale.

4.4.1 Boundary Conditions

Some boundary conditions for the model geometry are given by Dussoubs et al. (2003) (10), while others are adapted for the purposes of this work. A summary of boundary conditions is provided in **Table 14** and **Table 15**.

Table 14 – Boundary conditions used in the model – horizontal section.

Edge/Position	Boundary Conditions
Solids entrance(*)	$F_{0,UO2} = 6.519 * 10^{-3}; F_{0,UF4} = 1.283 * 10^{-2};$ $T_{0,s} = 573$
Gas entrance	$F_{0,H2O} = 0; F_{0,HF} = 4.252 * 10^{-1};$ $T_{0,g} = 523$

(*) Obtained from the results of the vertical section.

Table 15 – Boundary conditions used in the model – vertical section.

Edge	Boundary Conditions
E6	$\rho_t = \rho_{UO3} = 1.57 * 10^3$ $\rho_{UO2} = \rho_{U3O8} = \rho_{UO2F2} = \rho_{UF4} = 0$ $p = 1.013 * 10^5$
E11	T = 973
E9	$c_i = c_{i,PFR}$ (for NH_3, H_2 and N_2 only)
E10	$T(r = R_{0,red}) = \frac{(\mathbf{h_{ext}}\mathbf{T_{ext}} + hT)}{(\mathbf{h_{ext}} + h)}$
E3, E4, E5	T = 300
E2	T = 460
E1(*)	$c_t = 2.198 * 10^1$ $c_{H2O} = 1.15;\ c_{HF} = 6.88$ T = 573
E12, E13, E14, E15	$\nabla\rho_i = \mathbf{D_r}\frac{\partial c_i}{\partial x} + \mathbf{D_z}\frac{\partial c_i}{\partial y} = \nabla T = \nabla p = 0$

Source: Adapted from [10].
(*) Obtained from the results of the horizontal section.

4.5. SOLVING THE MODEL

This section contains the strategies used in the code to reduce computational efforts, such as initial guesses (or initial solutions) and the mesh used to discretize the model. All tolerances (absolute, residual and relative) were set to $1x10^{-3}$, and the maximum number of iterations was set to 50.

According to the software documentation, MATLAB®, by default, discretizes the problem geometry using triangles, in the case of a two dimensional model. Then, it uses the Newton iterations in each node (formed by each triangle vertex) in order to find the solution for the entire model (57).

4.5.1. Initial Guess

For the initial guess, either a constant value or a function of position was considered in every solution node. **Table 16** presents in more detail the guesses used for each variable in the model.

Table 16 – Initial guess used in the model.

Face	Variable	Initial Guess	Face	Variable	Initial Guess
F3	ρ_t, ρ_{UO3}, ρ_{UO2}, ρ_{U3O8}	$1.57 * 10^3 * (1 - \frac{y}{L})$	F2 (cont.)	c_{H2O}	3.29
	ρ_{UO2F2}, ρ_{UF4}, c_{H2O}, c_{HF}	0		c_{HF}	2.60
	c_t	$1.523 * 10^1 * (1 + \frac{y}{L})$		T	445
	c_{NH3}	$9.42 * 10^0 * (1 - \frac{y}{L})$	F1	ρ_t	$2.238 * 10^3$
	c_{N2}	$1.45 * 10^0 * (1 + \frac{y}{L})$		ρ_{UO2}, ρ_{UF4}	$7.0 * 10^2$
	c_{H2}	$4.36 * 10^0 * (1 + \frac{y}{L})$		ρ_{UO3}, ρ_{U3O8}, ρ_{UO2F2}	0
	T	900		c_t	$2.127 * 10^1$
F2	ρ_t	$1.492 * 10^3$		c_{H2O}	$1.325 * 10^1$
	ρ_{UO2}	$1.4 * 10^3$		c_{HF}	5.30
	ρ_{UO2F2}	$1.475 * 10^2$		T	400
	ρ_{UO3}, ρ_{U3O8}, ρ_{UF4}	0	F1, F2	c_{H2}, c_{N2}, c_{NH3}	0
	c_t	$1.864 * 10^1$	F1, F2, F3	p	$1.013 * 10^5$

4.5.2. Mesh

In order to make a compromise between computational time and reliability in the results, a maximum element size of $0.4*R_0$ was considered, while a minimum element size of $0.01*R_0$ was applied, resulting in a mesh comprised of $2.015*10^3$ nodes total. This configuration allowed for approximately 45 minutes of run time using a computer with an AMD Phenom II X4 945 3.0 GHZ Quad-core processor.

5. RESULTS AND DISCUSSION

This section presents the results obtained by solving the PDEs and nonlinear equations of the model, taking into account the geometry and boundary conditions. In order to facilitate a comparison with the existing literature, the results are presented as longitudinal "cuts" of each zone (which is possible due to symmetry), with the radial dimensions varying between 0 (symmetry axis) and R_0, and the longitudinal dimensions varying between 0 and L. Since the existing literature provides models that assumed different premises and/or left some parameters values undisclosed, only a qualitative analysis will be performed.

5.1. REDUCTION ZONE

Figure 10 exhibits plots for the total solid density, as well as for each compound present in this phase. **Figure 10(a)** displays a change in total solids density along the equipment, which is expected due to the increase in UO_2 (whose density is lower than the solids density in the feed) mass fraction in this phase.

Figure 10(b) and **Figure 10(c)** exhibit the density of the initial reactant and product of the reduction reactions (UO_3 and UO_2, respectively). According to these plots, the reduction reactions occur at the top of the reactor and, since these compounds are quickly consumed (or produced), it can be inferred that the reactions occur completely and rapidly at the temperatures in this specific area of the furnace, which is expected, as described in the section 2.2.1 of this work.

Figure 10(d) also shows the intermediate compound (U_3O_8) being produced and quickly consumed, as evidenced by the low maximum density values achieved. This behavior is typical for compounds present in reactions including its production and consumption in the same system. The short length in which change in density for the reactants is observed indicates the reduction reactions occur quickly.

Figure 10(e) indicates the undesirable compound (UO_2F_2) being produced due to reaction with the HF that remained from the lower sections of the furnace. It can also be observed that the secondary hydrofluorination reaction occurs more evidently near the symmetry axis.

Figure 10(f) shows that the hydrofluorination reaction does not occur in this section of the furnace, since no UF_4 was produced, which was also expected according to the section 2.2.1.

Figure 10 – Solid density plots for the reduction zone, m x kg/m^3. (a) Apparent (total) solids density of the bed; (b) UO_3; (c) UO_2; (d) U_3O_8; (e) UO_2F_2; and (f) UF_4.

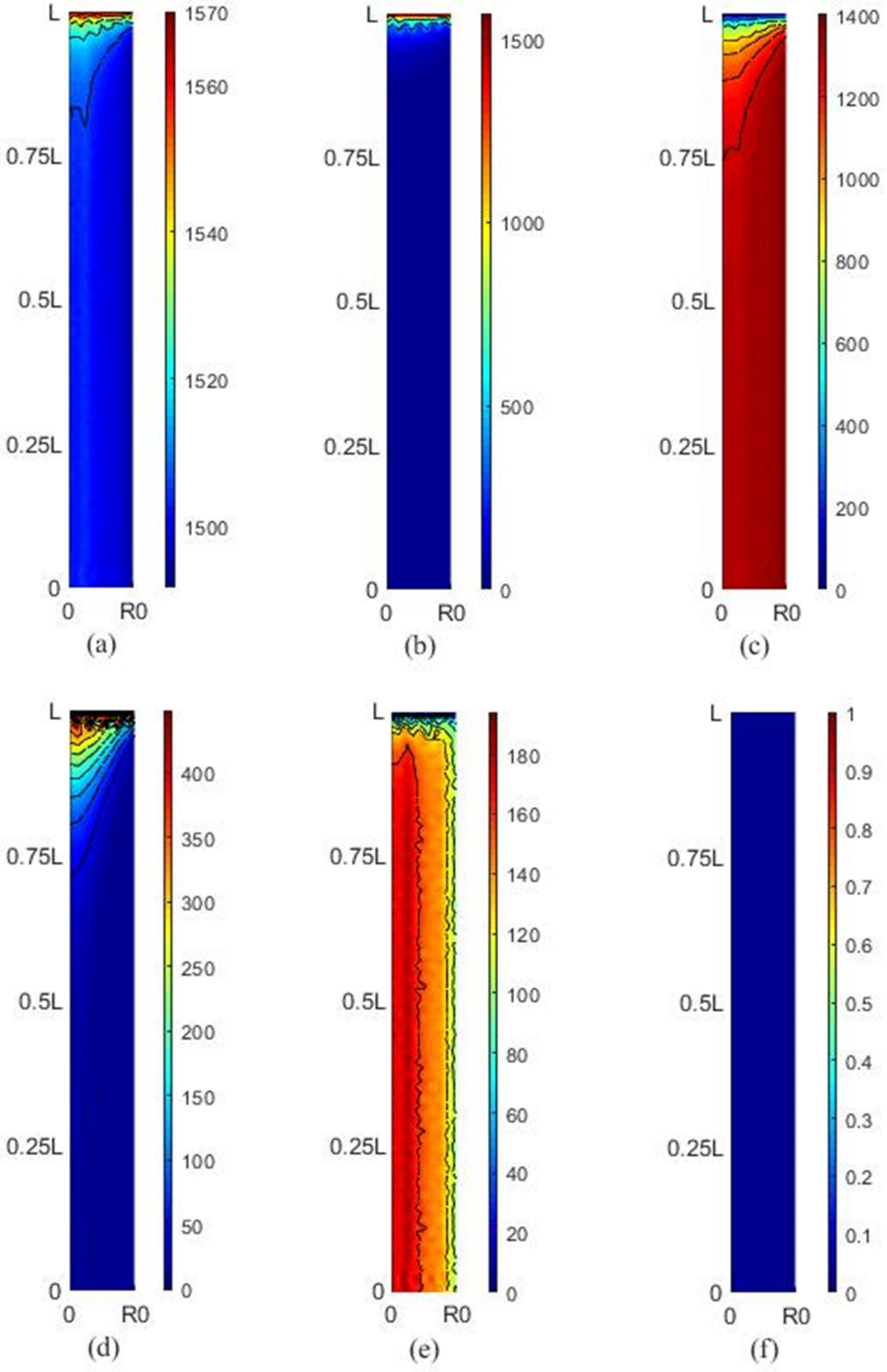

The obtained results are in accordance with the ones presented in the work by Dussoubs et al. (2003) (12), which shows the complete conversion occurring in the very top of the zone. It should be stated that this reference shows the completion needing a longer length to be achieved, but this is due to the fact that the muffle does not envelop the whole zone, since the reaction starts as soon as the solid enters the muffle heated region.

The concentration of gases inside this zone is shown in **Figure 11**. As disclosed in section 4.4, the bottom of each plot represents the entrance of cracked NH_3. Since the literature does not provide plots for the gaseous phase, the analysis of this group of variables will be limited to comparing results with other variables within the model of this work.

Figure 11(a) shows the total concentration of the gas phase, and changes can be observed near the top of the section close to the walls mainly due to the contribution of N_2 and H_2, which are products of the cracking reaction.

Figure 11(b) and **Figure 11(c)** represent, respectively, the reactant and one of the products (N_2) of the cracking reaction, and it can be seen they contrast each other, i.e., areas that show a higher concentration of product show a lower concentration of reactant. Although **Figure 11(d)** also represents the concentration of the other product of the cracking reaction (H_2), it does not have the same behavior of the N_2, since the former is consumed in the reduction reactions, mostly in the top of the furnace, which explain the profile of this compound.

Figure 11(e) shows an increasing concentration of H_2O vapor due to the production of this compound in the reduction reactions. The areas in which the concentrations are higher match the one where these reactions are most prominent according to **Figure 10**, i.e., the top of the equipment.

Figure 11(f) exhibits the concentration of HF. Its decrease near the top of the furnace can be explained due to its consumption in the secondary hydrofluorination reaction.

As seen in **Figure 11**, the cracking of ammonia occurs mainly near the walls. This is in accordance to the conclusions of Dussoubs et al. (2003) (12), which states that this reaction is expressive in temperatures above 600 ºC. This leads to an increased production of N_2 and H_2 in this region; however, since H_2 participates in the reduction reactions, the area in which the concentration of each gas is higher is slightly different. As for H_2O and HF, their plots correctly represent the area in which the reactions occur (top of the zone).

Figure 11 – Gas density plots for the reduction zone, m x mol/m^3. (a) Total gas concentration; (b) NH_3; (c) N_2; (d) H_2; (e) H_2O; and (f) HF.

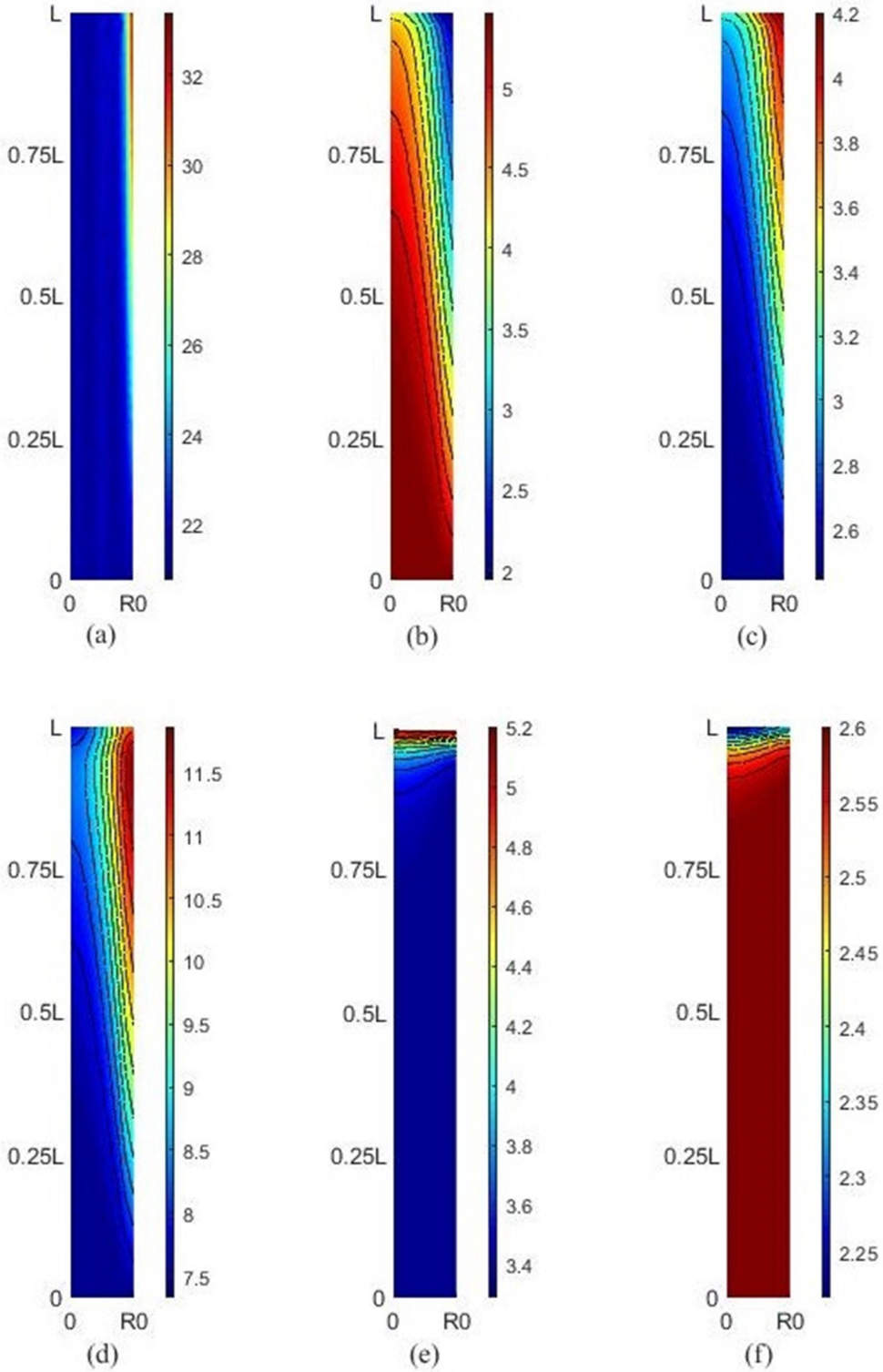

The temperature profile of this zone is presented in **Figure 12**.

Figure 12 – Temperature profile of the reduction zone, m x K.

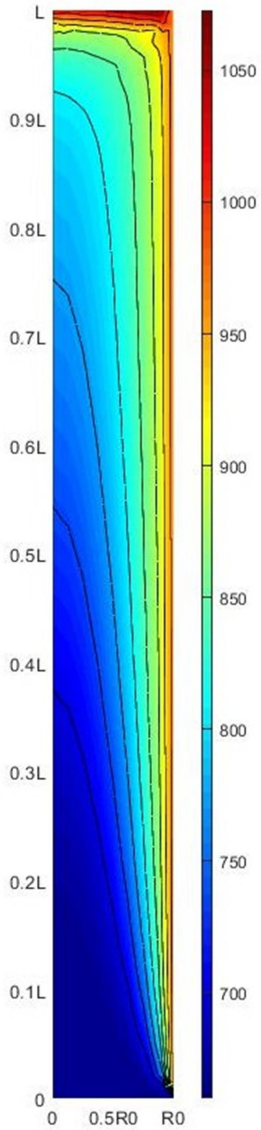

As seen in **Figure 12**, the temperature increases axially from bottom to top; however, the results are not in total agreement to the literature data (Dussoubs et al. (12)), indicating that the region in which the reactions occur most intensely is not at the very top of the furnace as reported, but at approximately 90% of its length. This is due to the fact that, in this work, the muffle surrounds the entire zone, which is not considered in the reported work. Another reason is the high temperature in which NH_3 is fed to the furnace, which is taken into account in this work, but it does not seem to be considered in the reported work. Despite this, the results obtained in this work are in accordance to the plots in the literature, indicating that the areas with higher temperatures coincide with the areas whose kinetic activity is highest, which

is expected for reactions not limited by thermodynamic equilibrium, in the top of the furnace, as well as near the walls, where the muffle is located.

5.2. BUFFER ZONE

Since there is no NH_3 (and, consequently, no H_2) in this zone and the temperatures are relatively low for the hydrofluorination reaction to take place in a significant way, changes are not expected in variables beside temperature. This is in accordance to the literature (Dussoubs et al. (12)), and is confirmed by **Figure 13** and **Figure 14**.

Figure 13 – Solid density plots for the buffer zone, m x kg/m^3. (a) Apparent (total) solids density of the bed; (b) UO_3; (c) UO_2; (d) U_3O_8; (e) UO_2F_2; and (f) UF_4.

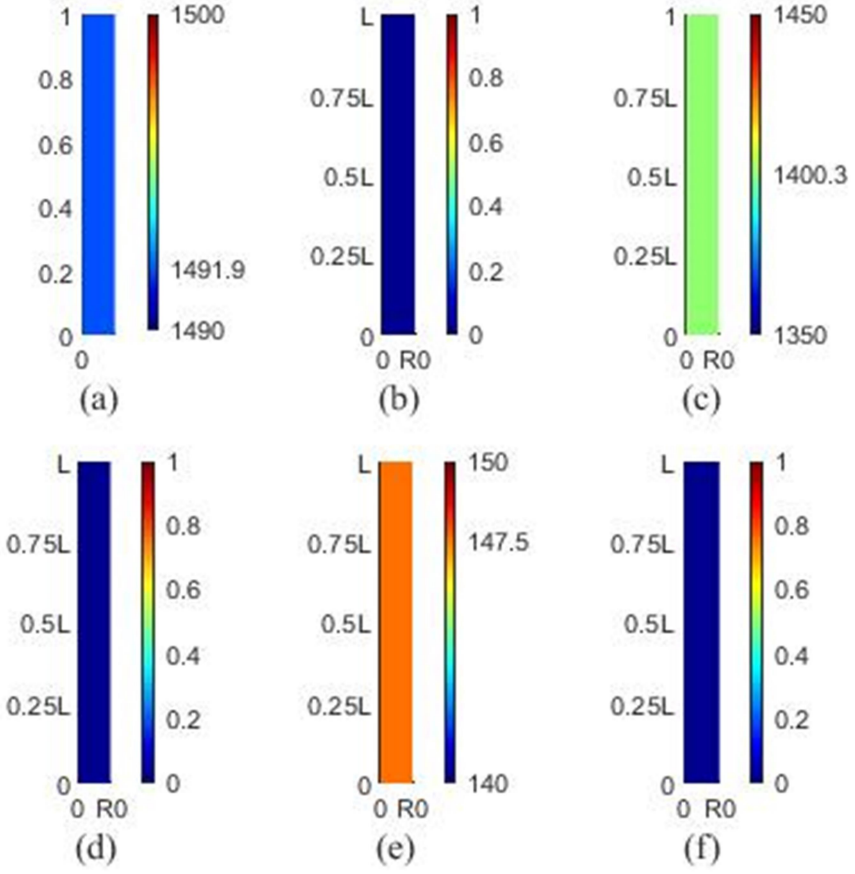

Figure 14 – Gas density plots for the buffer zone, m x mol/m^3. (a) Total gas concentration; (b) NH_3; (c) N_2; (d) H_2; (e) H_2O; and (f) HF.

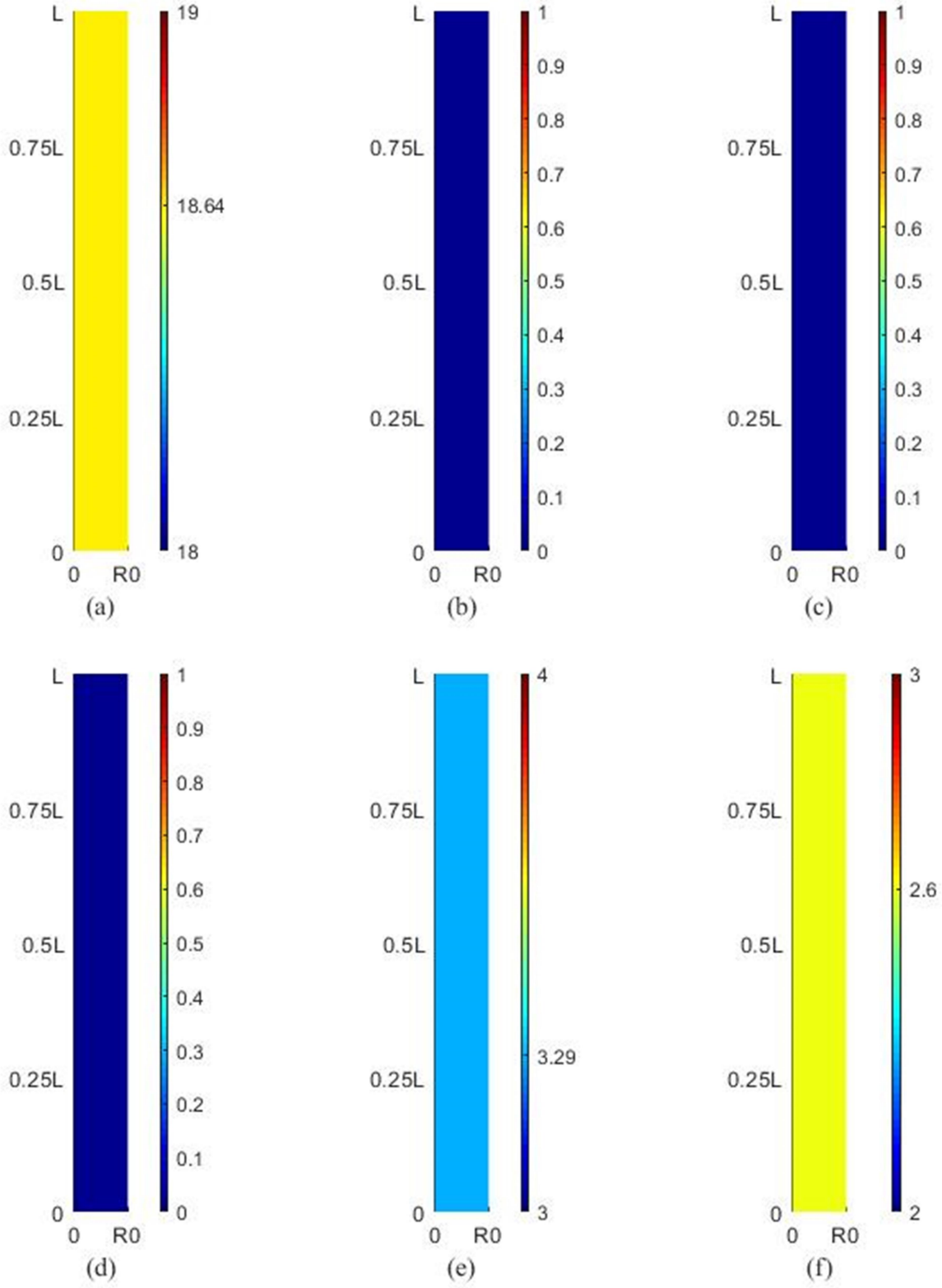

The temperature profile for this zone is shown in **Figure 15**. Since no reactions occur, it can be inferred that the temperature decrease is due to the exposition of the outer walls to the ambient temperature. This explains the fact that lower temperatures are prevalent in the area closer to the wall, and higher temperatures are closer to the center (symmetry axis).

Figure 15 – Temperature profile of the buffer zone, m x K.

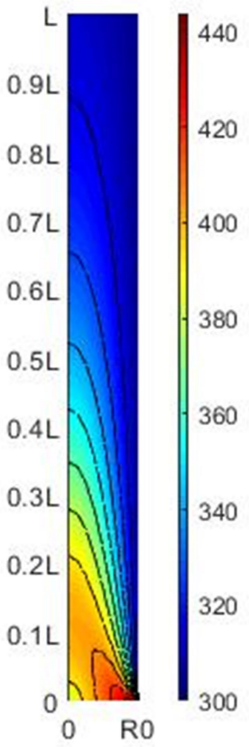

5.3. VERTICAL HYDROFLUORINATION ZONE

Solid density plots for the vertical hydrofluorination zone are presented in **Figure 16**. Since the densities for UO_3, UO_2F_2 and U_3O_8 retain the same values than the previous zone (no reactants available for the reduction reactions), they will be omitted.

Figure 16(a) shows the total solids density of the bed. The increase in total density can be expected, since UF_4, which is the product of the reaction that occurs in this section, increases in composition along this section, has higher density than the solid reactant (UO_2).

Figure 16(b) and **Figure 16(c)** show the density of the reactant and product of the hydrofluorination reaction, respectively. These two figures are complementary to each other, i.e., regions rich in reactant are poor in product, and vice versa, which is expected, since this

section has only one reaction. It can also be observed that this reaction does not occur completely, since some quantity of reactant is still present at the bottom of the section.

Figure 16 – Solid density plots for the vertical hydrofluorination zone, m x kg/m^3. (a) Apparent (total) solids density of the bed; (b) UO_2; and (c) UF_4.

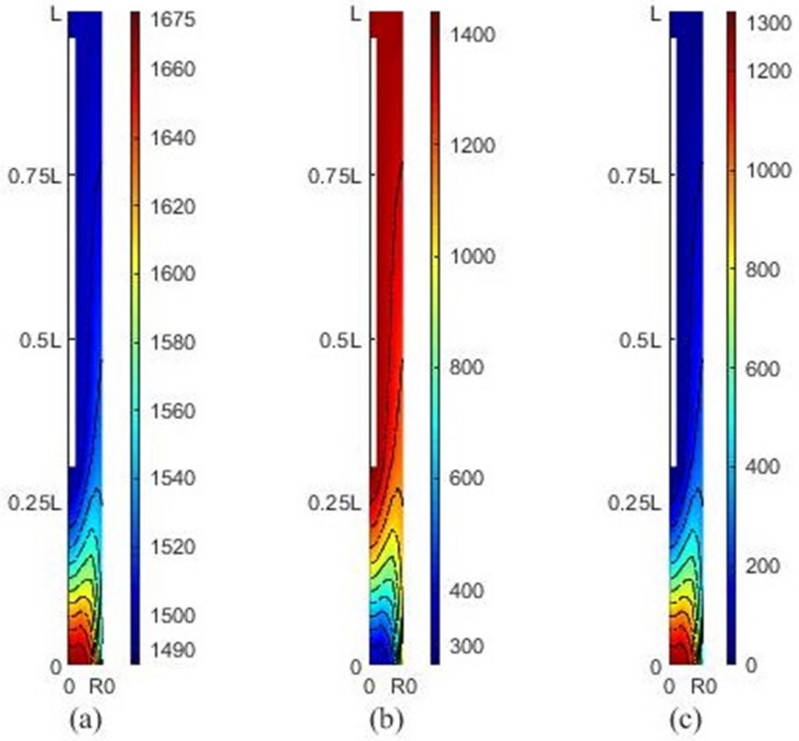

The results found in this work mostly agree with the existing literature. The main exception is in top of the zone, which shows that the hydrofluorination reaction also takes place in the area before the heat exchanger in the cited reference. This deviation is due to the fact that a muffle is used for the zone in this work, and the feed parameters (UO_3 and HF flow rate and temperature) are different. However, both works agree on the observation that the reaction seems to be more pronounced near the walls, where the UF_4 fraction of the solids is greater.

In order to complement the solid density plots for this zone, **Figure 17** shows the gas concentration plots obtained by the model.

Figure 17(a) exhibits the total concentration of the gas phase. Its variation along this vertical section is due to the consumption of HF in the hydrofluorination reaction. Although H_2O vapor is also produced, the consumption of the other gas species is more prominent due to the reaction stoichiometry, and the net result is a decreased concentration in the top of this section of the furnace.

Figure 17 – Gas density plots for the vertical hydrofluorination zone, m x mol/m^3. (a) Total gas concentration; (b) H_2O; and (c) HF.

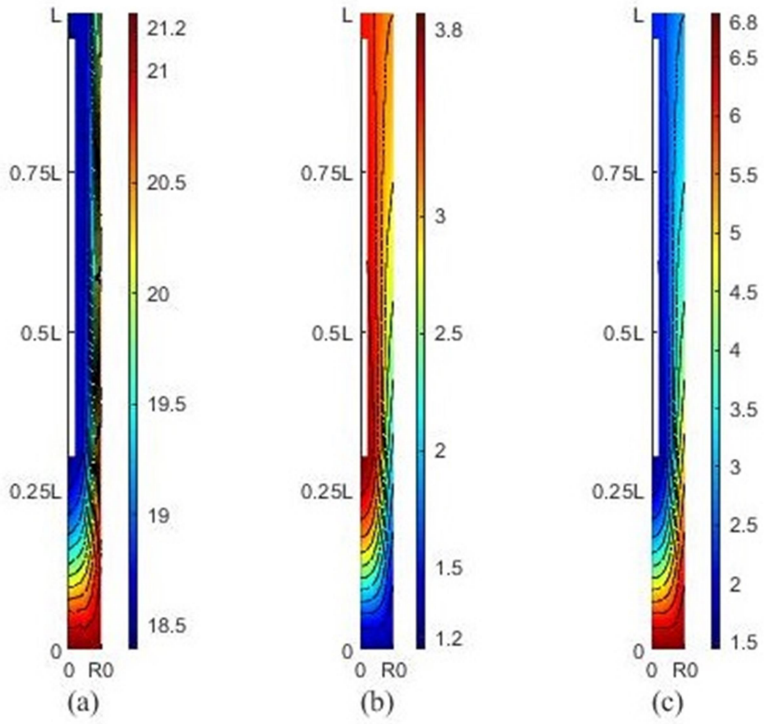

Figure 17(b) and **Figure 17(c)** show the concentration of the gas species involved in the hydrofluorination reaction, and, similarly to **Figure 16(b)** and **Figure 16(c)**, they also complement each other.

Although there is no available data to perform a comparison with other works in the literature, the areas that show a higher HF consumption (or higher H_2O production) are observed to be also the ones that show high UF_4 density in the **Figure 16(c)**, indicating the model in this work shows logical sense.

The plot showing the temperature profile for this zone is presented in **Figure 18**.

The results show that the temperature increases from top to bottom in the furnace, with the highest temperature gradients occurring near the walls (both exterior and for the heat exchanger), with the walls of the heat exchanger exhibiting an important cooling effect, which is an observation also applicable to the results found in this work. The remark that the hottest zones do not coincide with the areas with higher UF_4 content (at about 400 ºC), due to the thermodynamic equilibrium is also pertinent here. These findings are in agreement with those reported by Dussoubs et al. (2003) (12).

Figure 18 – Temperature profile of the vertical hydrofluorination zone, m x K.

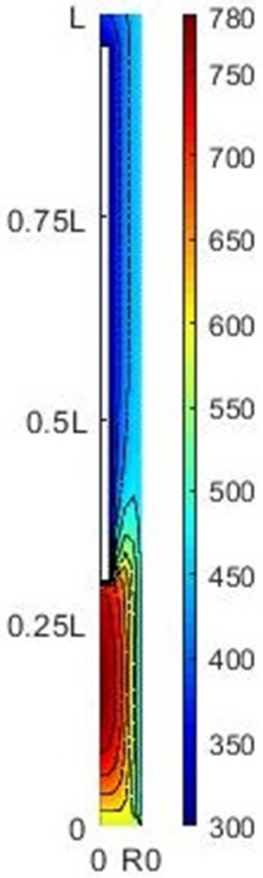

5.4. PRESSURE

The last variable analyzed for the vertical section of the furnace in this work is the pressure drop for the gaseous phase, and it is represented in **Figure 19.**

Although the graph shows that a pressure drop does occur for the gas phase flow, its magnitude is almost insignificant (at most 1.2% in the end of the vertical hydrofluorination zone), so that we can infer that the pressure remains constant in the region studied by this work. This result is in accordance to Dussoubs et al. (10), which states that the pressure drop throughout the furnace bed is relatively low.

Figure 19 – Pressure plots for the vertical section of the furnace, m x Pa. (a) Reduction zone; (b) Buffer zone; and (c) Vertical Hydrofluorination zone.

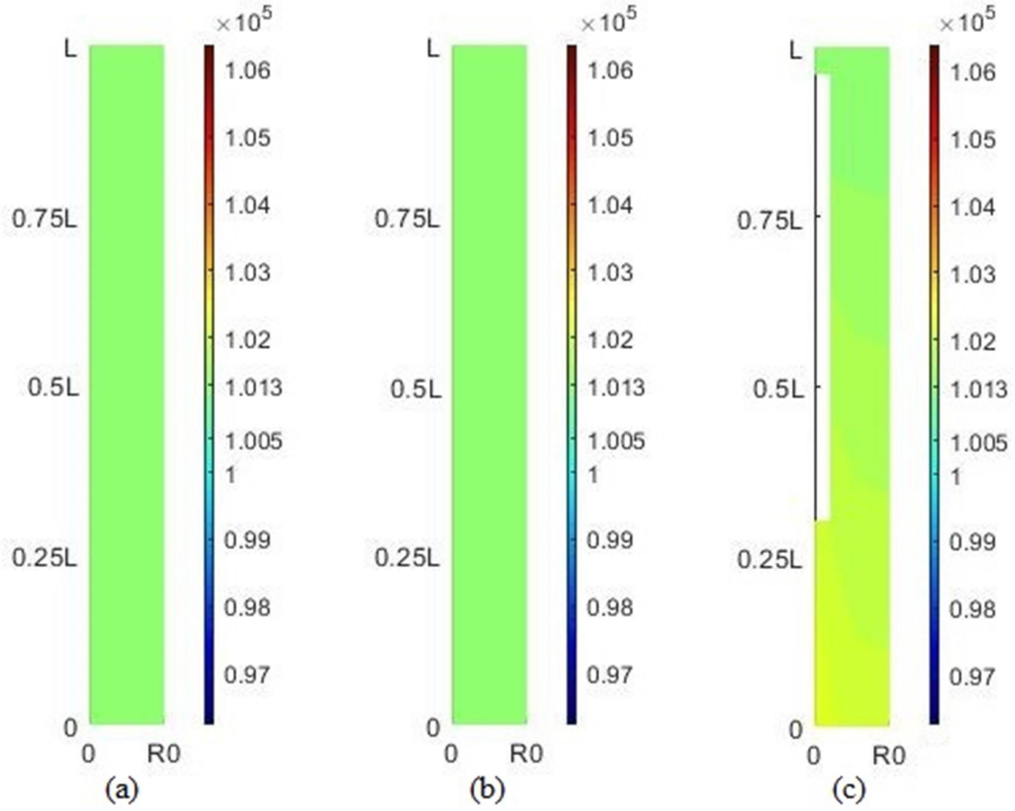

5.5. HORIZONTAL SECTION

Lastly, the horizontal hydrofluorination zone is responsible for concluding the hydrofluorination reaction. **Figure 20** summarizes the results for the solid and gaseous phases. Only information regarding the reacting/produced species is shown, while the rest is omitted since they remain the same as the end of the vertical hydrofluorination zone.

Figure 20 shows that the incomplete reaction at the bottom of the vertical zone continues, and the increase in product (or decrease in reactant) is approximately linear up to the end of the zone.

Also, as seen in the **Figure 20**, the reaction is concluded due to the lack of UO_2 in the last CSTR, right before the solids exit (or gas entrance). This is in accordance to Dussoubs et al. (12) and Niksiar and Rahimi (13), which also show conversion close to unity in this position. In terms of product purity, the value found in this work is approximately 92%.

Figure 20 – Density and concentration plots for the horizontal hydrofluorination zone. (a) Solid phase, CSTR number x kg/m^3; (b) Gaseous phase, CSTR number x mol/m^3.

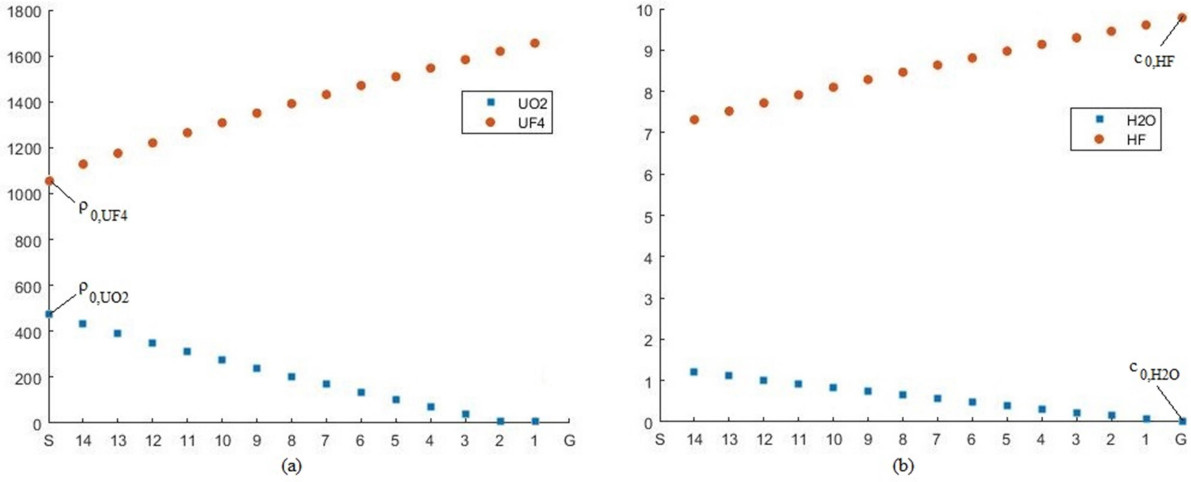

Note: "S" denotes solids feed and "G" denotes HF feed.

As for temperature for each phase, **Figure 21** shows the results of the heat balances.

Figure 21 – Temperature plots for the horizontal hydrofluorination zone, CSTR number x K. (a) Solid phase; (b) Gaseous phase.

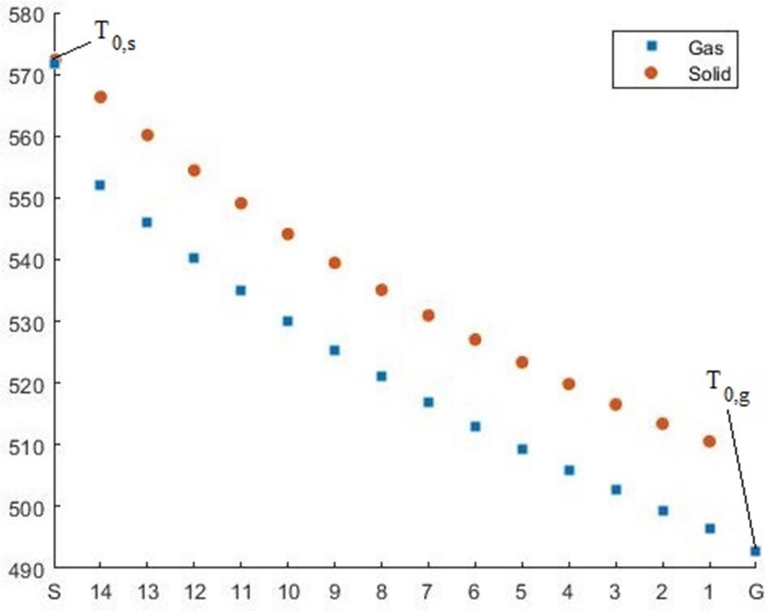

Note: "S" denotes solids feed and "G" denotes HF feed.

As seen in **Figure 21**, the temperature decreases along the horizontal section, mainly due to the proximity of the gas feed, which exhibits a lower temperature, while neither the

heat of reaction nor the muffle produce enough heat to maintain the solids feed temperature in this part of the furnace.

The behavior of this variable seems to mainly agree with the reference articles, in that both temperatures drop along the length of the zone, however, Dussoubs et al. (12) and Niksiar and Rahimi (13) show an initial temperature increase, as well as the difference between phase temperatures being smaller near the solids entrance. This can be explained due to the relatively low temperatures found for this work in this region, as this effect is mitigated with its increase.

It should also be stated that the temperature of the muffle does not significantly alter the values for this variable, with the initial temperature of the solids phase being the main source of overall temperature increase in this section. This behavior was also observed in Dussoubs et al. (12).

6. CONCLUSIONS

A model describing the conversion of UO_3 into UF_4, including mass, momentum and energy balances in a moving bed reactor, which is a major component in the nuclear fuel cycle, was successfully developed.

The results show a good agreement with the reported literature and deviation was mainly by the different correlations, as well as different configurations, such as an extra muffle in the vertical hydrofluorination zone, used in this work, in order to find parameters which were not given or were not entirely clear in the reference models reported in the literature.

This work contributes to the existing literature by including correlations presented in more recent works and combining expressions used in different existing models. Also, a method to calculate the composition of NH_3 fed into the reactor using readily available operating conditions (pressure and temperature) was disclosed. Data regarding gas phase concentrations, which is scarce in literature, was also presented in this work.

7. SUGGESTIONS FOR FUTURE WORKS

As further contribution to this field, the following suggestions can be made, in no particular order of relevance:

- Include the kinetics for the calcination reaction, since no data has been found in the literature, besides the fact that it indeed occurs in the process;

- Compare the model with data found during the operation of the equipment;

- Include calculations for the transient state; and

- Include calculations with different meshes (element sizes and tolerances);

REFERENCES*

1. AGÊNCIA CÂMARA DE NOTÍCIAS. Deputados apoiam comissão mista para acompanhar ações na Amazônia Azul. [online]. 2017. Available from: https://www.camara.leg.br/noticias/513085-deputados-apoiam-comissao-mista-para-acompanhar-acoes-na-amazonia-azul/
2. ANDRADE, I. O., FRANCO E SILVA, M. M. F., HILLEBRAND, G. R. L., FRANCO, L. G. A. *Submarino Nuclear Brasileiro: Defesa Nacional e Externalidades Tecnológicas* [online]. 2018. Available from: http://repositorio.ipea.gov.br/bitstream/11058/8904/1/td_2428.pdf
3. COSTA, Eugenio Pacelli Lazzarotti Diniz. Brazil's Nuclear Submarine: A Broader Approach to the Safeguards Issue. *Revista Brasileira de Política Internacional* [online]. 19 October 2017. Vol. 60, no. 2. DOI 10.1590/0034-7329201700205. Available from: http://www.scielo.br/scielo.php?script=sci_arttext&pid=S0034-73292017000200202&lng=en&tlng=en
4. COMMISSARIAT À L'ÉNERGIE ATOMIQUE ET AUX ENERGIES ALTERNATIVES. *The nuclear fuel cycle* [online]. 2005. Available from: http://www.cea.fr/english/Documents/thematic-publications/nuclear-fuel-cycle.pdf
5. INTERNATIONAL ATOMIC ENERGY AGENCY. *Technical Report Series no. 425: Country Nuclear Fuel Cycle Profiles* [online]. 2005. Available from: https://www-pub.iaea.org/MTCD/publications/PDF/TRS425_web.pdf
6. INTERNATIONAL ATOMIC ENERGY AGENCY. *Nuclear Fuel Cycle Information System* [online]. 2009. Available from: https://www-pub.iaea.org/MTCD/publications/PDF/te_1613_web.pdf
7. OLIVER, A.J., ÖZBERK, E. Uranium for Nuclear Power. In : [online]. Elsevier, 2016. p. 299–319. ISBN 9780081003077. Available from: https://linkinghub.elsevier.com/retrieve/pii/C20140033096
8. EDWARDS, C. R. and OLIVER, A. J. Uranium processing: A review of current methods and technology. *JOM* [online]. September 2000. Vol. 52, no. 9, p. 12–20. DOI 10.1007/s11837-000-0181-2. Available from: http://link.springer.com/10.1007/s11837-000-0181-2

* The ISO-690 (Numeric System) was used as standard for this work

9. OAK RIDGE NATIONAL LABORATORY. *Model of a Generic Natural Uranium Conversion Plant - Suggested Measures to Strengthen International Safeguard* [online]. 2009. Available from: https://info.ornl.gov/sites/publications/files/Pub13143.pdf

10. DUSSOUBS, B., JOURDE, J., PATISSON, F., HOUZELOT, J.-L. and ABLITZER, D. Modelling of a moving bed furnace for the production of uranium tetrafluoride Part 1: formulation of the model. *Chemical Engineering Science* [online]. June 2003. Vol. 58, no. 12, p. 2617–2627. DOI 10.1016/S0009-2509(03)00117-9. Available from: https://linkinghub.elsevier.com/retrieve/pii/S0009250903001179

11. DUSSOUBS, B, JOURDE, J, PATISSON, F, HOUZELOT, J.L and ABLITZER, D. Mathematical modelling of uranium dioxide conversion in a moving bed furnace. *Powder Technology* [online]. December 2002. Vol. 128, no. 2–3, p. 168–177. DOI 10.1016/S0032-5910(02)00194-8. Available from: https://linkinghub.elsevier.com/retrieve/pii/S0032591002001948

12. DUSSOUBS, B., JOURDE, J., PATISSON, F., HOUZELOT, J.-L. and ABLITZER, D. Modelling of a moving bed furnace for the production of uranium tetrafluoride. Part 2: Application of the model. *Chemical Engineering Science* [online]. June 2003. Vol. 58, no. 12, p. 2629–2642. DOI 10.1016/S0009-2509(03)00121-0. Available from: https://linkinghub.elsevier.com/retrieve/pii/S0009250903001210

13. NIKSIAR, Arezou and RAHIMI, Amir. Design of a moving bed reactor for the production of uranium tetrafluoride based on mathematical modeling. *Chemical Engineering Science* [online]. May 2010. Vol. 65, no. 10, p. 3147–3157. DOI 10.1016/j.ces.2010.02.004. Available from: https://linkinghub.elsevier.com/retrieve/pii/S0009250910000709

14. NIKSIAR, Arezou and RAHIMI, Amir. On the validity of the rate expression of calcination reaction of UO3 reported by Dussoubs et al. (2003). *Chemical Engineering Science* [online]. February 2009. Vol. 64, no. 3, p. 618–619. DOI 10.1016/j.ces.2008.10.033. Available from: https://linkinghub.elsevier.com/retrieve/pii/S0009250908006040

15. BYKOV, A.A., TRAVIN, S.O., GROMOV, O.B. and MIKHEEV, P.I. Modeling of Uranium Oxides Hydrofluorination Process with AREVA Firm Technology (Malvési, France). *Procedia Chemistry* [online]. 2014. Vol. 11, p. 3–9. DOI 10.1016/j.proche.2014.11.002. Available from:

https://linkinghub.elsevier.com/retrieve/pii/S1876619614001521

16. RAHIMI, Amir and NIKSIAR, Arezou. A general model for moving-bed reactors with multiple chemical reactions part I: Model formulation. *International Journal of Mineral Processing* [online]. November 2013. Vol. 124, p. 58–66. DOI 10.1016/j.minpro.2013.02.015. Available from: https://linkinghub.elsevier.com/retrieve/pii/S0301751613000628

17. TAKENAKA, Y., KIMURA, Y., NARITA, K. and KANEKO, D. Mathematical model of direct reduction shaft furnace and its application to actual operations of a model plant. *Computers & Chemical Engineering* [online]. January 1986. Vol. 10, no. 1, p. 67–75. DOI 10.1016/0098-1354(86)85047-5. Available from: https://linkinghub.elsevier.com/retrieve/pii/0098135486850475

18. RAHIMI, Amir and NIKSIAR, Arezou. A general model for moving-bed reactors with multiple chemical reactions, Part II: Effect of kinetic model. *International Journal of Mineral Processing* [online]. November 2013. Vol. 124, p. 67–74. DOI 10.1016/j.minpro.2013.06.003. Available from: https://linkinghub.elsevier.com/retrieve/pii/S0301751613001397

19. VALIPOUR, Mohammad Sadegh and SABOOHI, Yadollah. Modeling of multiple noncatalytic gas–solid reactions in a moving bed of porous pellets based on finite volume method. *Heat and Mass Transfer* [online]. 24 May 2007. Vol. 43, no. 9, p. 881–894. DOI 10.1007/s00231-006-0154-2. Available from: http://link.springer.com/10.1007/s00231-006-0154-2

20. USUI, Tateo, OHMI, Munekazu and YAMAMURA, Eiji. Analysis of rate of hydrogen reduction of porous wustite pellets basing on zone-reaction models. *ISIJ International* [online]. 1990. Vol. 30, no. 5, p. 347–355. DOI 10.2355/isijinternational.30.347. Available from: http://joi.jlc.jst.go.jp/JST.Journalarchive/isijinternational1989/30.347?from=CrossRef

21. POULESQUEN, A. and VERGNES, B. A study of residence time distribution in co-rotating twin-screw extruders. Part I: Theoretical modeling. *Polymer Engineering & Science* [online]. December 2003. Vol. 43, no. 12, p. 1841–1848. DOI 10.1002/pen.10156. Available from: http://doi.wiley.com/10.1002/pen.10156

22. KUMAR, Ajay, GANJYAL, Girish M., JONES, David D. and HANNA, Milford A. Modeling residence time distribution in a twin-screw extruder as a series of ideal

steady-state flow reactors. *Journal of Food Engineering* [online]. February 2008. Vol. 84, no. 3, p. 441–448. DOI 10.1016/j.jfoodeng.2007.06.017. Available from: https://linkinghub.elsevier.com/retrieve/pii/S0260877407003445

23. SHI, Xiaogang, RONSSE, Frederik, NACHENIUS, Robert and PIETERS, Jan G. 3D Eulerian-Eulerian modeling of a screw reactor for biomass thermochemical conversion. Part 2: Slow pyrolysis for char production. *Renewable Energy* [online]. December 2019. Vol. 143, p. 1477–1487. DOI 10.1016/j.renene.2019.05.088. Available from: https://linkinghub.elsevier.com/retrieve/pii/S096014811930761X

24. SHI, Xiaogang, RONSSE, Frederik, ROEGIERS, Jelle and PIETERS, Jan G. 3D Eulerian-Eulerian modeling of a screw reactor for biomass thermochemical conversion. Part 1: Solids flow dynamics and back-mixing. *Renewable Energy* [online]. December 2019. Vol. 143, p. 1465–1476. DOI 10.1016/j.renene.2019.05.098. Available from: https://linkinghub.elsevier.com/retrieve/pii/S0960148119307712

25. SOHN, H. Y. The law of additive reaction times in fluid-solid reactions. *Metallurgical Transactions B* [online]. March 1978. Vol. 9, no. 1, p. 89–96. DOI 10.1007/BF02822675. Available from: http://link.springer.com/10.1007/BF02822675

26. PATISSON, F.; DUSSOUBS, B.; ABLITZER, D. Using Sohn's Law of Additive Reaction Times for Modeling a Multiparticle Reactor. The case of the moving bed furnace converting uranium trioxide into tetrafluoride. In : *Sohn International Simposium* [online]. 2006. p. 27–31. Available from: https://arxiv.org/ftp/arxiv/papers/0803/0803.2837.pdf

27. PATRICK, John W. *Handbook of fuel cells. Fundamentals technology and applications*. John Wiley & Sons, Ltd., 2004. A timely addition to the highly acclaimed four-volume handbook set; volumes 5 and 6 highlight recent developments, particularly in the fields of new materials, molecular modeling and durability. Since the publication of the first four volumes of the Handbook of Fuel Cells in 2003, the focus of fuel cell research and development has shifted from optimizing fuel cell performance with well-known materials to developing new materials concepts, and to understanding the origins of materials and fuel cell degradation. This new two-volume set provides an authoritative and timely guide to these recent developments in fuel cell research.

28. ITOH, Masahiro, MASUDA, Masahiro and MACHIDA, Ken-ichi. Hydrogen

Generation by Ammonia Cracking with Iron Metal-Rare Earth Oxide Composite Catalyst. *MATERIALS TRANSACTIONS* [online]. 2002. Vol. 43, no. 11, p. 2763–2767. DOI 10.2320/matertrans.43.2763. Available from: https://www.jstage.jst.go.jp/article/matertrans/43/11/43_11_2763/_article

29. POLANSKI, Jaroslaw, BARTCZAK, Piotr, AMBROZKIEWICZ, Weronika, SITKO, Rafal, SIUDYGA, Tomasz, MIANOWSKI, Andrzej, SZADE, Jacek, BALIN, Katarzyna and LELĄTKO, Józef. Ni-Supported Pd Nanoparticles with Ca Promoter: A New Catalyst for Low-Temperature Ammonia Cracking. BHARGAVA, Suresh (ed.), *PLOS ONE* [online]. 26 August 2015. Vol. 10, no. 8, p. e0136805. DOI 10.1371/journal.pone.0136805. Available from: https://dx.plos.org/10.1371/journal.pone.0136805

30. ELOIRDI, R., HO MER LIN, D., MAYER, K., CACIUFFO, R. and FANGHÄNEL, T. Investigation of ammonium diuranate calcination with high-temperature X-ray diffraction. *Journal of Materials Science* [online]. 9 December 2014. Vol. 49, no. 24, p. 8436–8443. DOI 10.1007/s10853-014-8553-0. Available from: http://link.springer.com/10.1007/s10853-014-8553-0

31. MANNA, Subhankar, KARTHIK, Phani, MUKHERJEE, Abhishek, BANERJEE, Joydipta, ROY, Saswati B. and JOSHI, Jyeshtharaj B. Study of calcinations of ammonium diuranate at different temperatures. *Journal of Nuclear Materials* [online]. July 2012. Vol. 426, no. 1–3, p. 229–232. DOI 10.1016/j.jnucmat.2012.03.035. Available from: https://linkinghub.elsevier.com/retrieve/pii/S0022311512001560

32. DELL, R. M. and WHEELER, V. J. Chemical reactivity of uranium trioxide. Part 1 — Conversion to U3O8 , UO2 and UF4. *Trans. Faraday Soc.* [online]. 1962. Vol. 58, p. 1590–1607. DOI 10.1039/TF9625801590. Available from: http://xlink.rsc.org/?DOI=TF9625801590

33. HEISKALA, Victor H. Kinetics of Hydrogen Reduction of Uranium Trioxide. *The Journal of Physical Chemistry* [online]. June 1965. Vol. 69, no. 6, p. 2012–2016. DOI 10.1021/j100890a035. Available from: https://pubs.acs.org/doi/abs/10.1021/j100890a035

34. LE PAGE, A.H. and FANE, A.G. The kinetics of hydrogen reduction of UO3 and U3O8 derived from ammonium diuranate. *Journal of Inorganic and Nuclear Chemistry* [online]. January 1974. Vol. 36, no. 1, p. 87–92. DOI 10.1016/0022-1902(74)80663-9. Available from: https://linkinghub.elsevier.com/retrieve/pii/0022190274806639

35. ALFARO, Pedro Orrego, TORRES, José Hernández and THIELE, Fernando Puchi. Reduction Kinetics of Uranium Trioxide to Uranium Dioxide Using Hydrogen. *World Journal of Nuclear Science and Technology* [online]. 2015. Vol. 05, no. 03, p. 149–156. DOI 10.4236/wjnst.2015.53015. Available from: http://www.scirp.org/journal/doi.aspx?DOI=10.4236/wjnst.2015.53015

36. PIJOLAT, M., BRUN, C., VALDIVESO, F., SOUSTELLE, M. Reduction of uranium oxide U3O8 to UO2 by hydrogen. *Solid State Ionics* [online]. November 1997. Vol. 101–103, p. 931–935. DOI 10.1016/S0167-2738(97)00385-8. Available from: https://linkinghub.elsevier.com/retrieve/pii/S0167273897003858

37. SIDOROV, E. V.; SOFRONOV, V. L. Investigation of the Kinetics of U3O8 Reduction by Hydrogen and Ammonia Under Non-Isothermal Conditions. *Chemistry for Sustainable Development*. 2011. Vol. 19, p. 315–319.

38. VALDIVIESO, Françoise, PIJOLAT, M, SOUSTELLE, M and JOURDE, J. Reduction of uranium oxide U3O8 into uranium dioxide UO2 by ammonia. *Solid State Ionics* [online]. May 2001. Vol. 141–142, p. 117–122. DOI 10.1016/S0167-2738(01)00730-5. Available from: https://linkinghub.elsevier.com/retrieve/pii/S0167273801007305

39. NOTZ, K.J. and MENDEL, M.G. X-ray and kinetic study of the hydrogen reduction of γ-UO3. *Journal of Inorganic and Nuclear Chemistry* [online]. July 1960. Vol. 14, no. 1–2, p. 55–64. DOI 10.1016/0022-1902(60)80199-6. Available from: https://linkinghub.elsevier.com/retrieve/pii/0022190260801996

40. NICOLE, Ch., PATISSON, F., ABLITZER, D. and HOUZELOT, J.-L. A thermogravimetric study of the kinetics of hydrofluorination of uranium dioxide. *Chemical Engineering Science* [online]. December 1996. Vol. 51, no. 23, p. 5213–5222. DOI 10.1016/S0009-2509(96)00271-0. Available from: https://linkinghub.elsevier.com/retrieve/pii/S0009250996002710

41. TOMLINSON, L., MORROW, Sheila A. and GRAVES, S. Kinetics of the hydrofluorination of uranium dioxide. *Transactions of the Faraday Society* [online]. 1961. Vol. 57, p. 1008. DOI 10.1039/tf9615701008. Available from: http://xlink.rsc.org/?DOI=tf9615701008

42. COSTA, Eduardo C. and SMITH, J. M. Kinetics of noncatalytic, nonisothermal, gas-solid reactions: Hydrofluorination of uranium dioxide. *AIChE Journal* [online]. July 1971. Vol. 17, no. 4, p. 947–958. DOI 10.1002/aic.690170431. Available from:

http://doi.wiley.com/10.1002/aic.690170431

43. GREEN, D. W.; SOUTHARD, M. Z. *Perry's Chemical Engineers' Handbook*. 9th Editio. McGraw-Hill Education, 2018.

44. HELD, P. C. *Emittance of uranium oxides*. Iowa State University, 1967.

45. CHAPLOT, S. L.; MITTAL, R. *Thermodynamic properites of solids: Experiment and modeling*. 1st Editio. Wiley-VCH, 2010.

46. PHILIP KOSKY, ROBERT BALMER, WILLIAM KEAT, and George Wise. *Exploring Engineering: An Introduction to Engineering and Design (Fourth Edition) - 978-0-12-801242-0*. 4th editio. Academic Press, 2015.

47. WACKER, P. F.; CHENEY, R. K. *Specific Heat, Enthalpy, and Entropy of Uranyl Fluoride*. 1947.

48. BRICKWEDDE, Ferdinand G., HOGE, Harold J. and SCOTT, Russell B. The Low Temperature Heat Capacities, Enthalpies, and Entropies of UF 4 and UF 6. *The Journal of Chemical Physics* [online]. May 1948. Vol. 16, no. 5, p. 429–436. DOI 10.1063/1.1746914. Available from: http://aip.scitation.org/doi/10.1063/1.1746914

49. FERREIRA NETO, R. A.; CAMARANO, D. M.; MIRANDA, O.; GROSSI, P. A.; CARNEIRO, L. C. S., SILVA, E. H. C.; MIGLIORINI, F. L.; AGUIAR, B. M.; BORGES, W. A.; SALIBA-SILVA, A. M. Uranium Tetrafluoride thermophysical properties measurements by the laser flash method. In : *International Nuclear Atlantic Conference*. 2013. p. 24–29.

50. MOORE, G. E.; KELLEY, K. K. High-Temperature Heat Contents of Uranium, Uranium Dioxide and Uranium Trioxide. *Journal of the American Chemical Society*. 1947. Vol. 69, no. 9, p. 2105–2107.

51. WILKE, C. R. A Viscosity Equation for Gas Mixtures. *The Journal of Chemical Physics* [online]. April 1950. Vol. 18, no. 4, p. 517–519. DOI 10.1063/1.1747673. Available from: http://aip.scitation.org/doi/10.1063/1.1747673

52. DWIVEDI, P. N. and UPADHYAY, S. N. Particle-Fluid Mass Transfer in Fixed and Fluidized Beds. *Industrial & Engineering Chemistry Process Design and Development* [online]. April 1977. Vol. 16, no. 2, p. 157–165. DOI 10.1021/i260062a001. Available from: https://pubs.acs.org/doi/abs/10.1021/i260062a001

53. RONCHI, C., SHEINDLIN, M., MUSELLA, M. and HYLAND, G. J. Thermal

conductivity of uranium dioxide up to 2900 K from simultaneous measurement of the heat capacity and thermal diffusivity. *Journal of Applied Physics* [online]. 15 January 1999. Vol. 85, no. 2, p. 776–789. DOI 10.1063/1.369159. Available from: http://aip.scitation.org/doi/10.1063/1.369159

54. VALIPOUR, M. S. Mathematical Modeling of a non-catalytic gassolid reaction: Hematite Pellet reduction with Syngas. *Transactions C: Chemical Engineering*. 2009. Vol. 16, no. 2, p. 108–124.

55. FOUMENY, Esmail A., CHOWDHURY, Masrur A., MCGREAVY, Colin and CASTRO, Jose A. A. Estimation of dispersion coefficients in packed beds. *Chemical Engineering & Technology* [online]. June 1992. Vol. 15, no. 3, p. 168–181. DOI 10.1002/ceat.270150305. Available from: http://doi.wiley.com/10.1002/ceat.270150305

56. FOGLER, H. S. *Elements of Chemical Reaction Engineering*. 5th editio. Prentice Hall, 2016.

57. MATHWORKS. Matlab Documentation - generateMesh. [online]. [Accessed 16 June 2020]. Available from: https://www.mathworks.com/help/pde/ug/pde.pdemodel.generatemesh.html